# MICROMECHANICS OF EPITHELIAL TISSUE - INSPIRED STRUCTURES

by

**Tejas Kulkarni**

**A Thesis**

*Submitted to the Faculty of Purdue University*

*In Partial Fulfillment of the Requirements for the degree of*

**Master of Science in Mechanical Engineering**

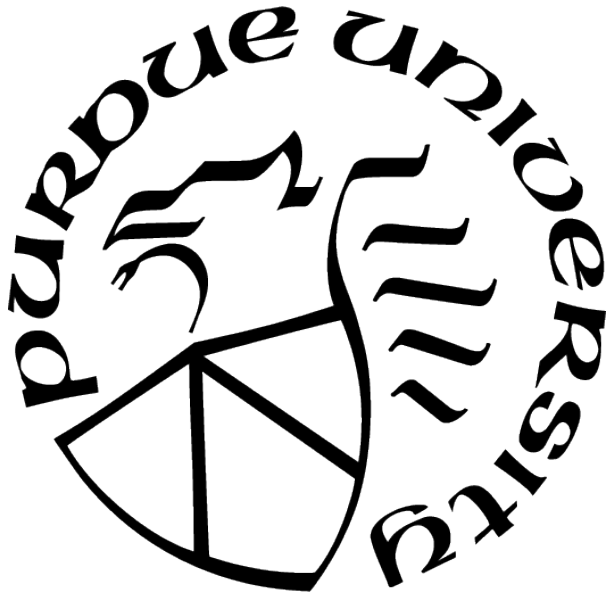


School of Mechanical Engineering

West Lafayette, Indiana

December 2021

# THE PURDUE UNIVERSITY GRADUATE SCHOOL
# STATEMENT OF COMMITTEE APPROVAL

**Dr. Adrian Buganza Tepole, Chair**

School of Mechanical Engineering

**Dr. Marcial Gonzalez**

School of Mechanical Engineering

**Dr. Andres Arrieta**

School of Mechanical Engineering

**Approved by:**

Dr. Nicole Key

# ACKNOWLEDGMENTS

I believe it is appropriate that I write this bit on the eve of Thanksgiving, acknowledging everyone who made this possible. First and foremost, I would like to express my sincere gratitude to my advisor, Dr. Adrian Buganza Tepole, who, over the course of my master's taught me the art of reasoning. His guidance on developing and testing various methods coupled with his expertise in continuum mechanics and non linear finite element modelling helped me immensely in making this study possible.

I would also like to thank my committee members, Dr. Marcial Gonzalez and Dr. Andres Arrieta for listening in on my research presentation and providing valuable constructive feedback on my methodology and findings.

I would also like to thank the entire Mechanical Engineering Department for supporting me during my Master's with a Teaching Assistant position. In addition to financial support, I also got the opportunity to interact and learn from an wide range of professors, and also their students. This experience was very enriching, and I cherish it greatly. Finally, I would like to extend my heartfelt gratitude to my family and friends. Their constant support and encouragement has played a significant role in making this possible. Thank you!

# TABLE OF CONTENTS

# LIST OF FIGURES

# ABSTRACT

Epithelial tissues, one of the four primary tissue structures found in our human body, are known to comprise of tiny cells interconnected in a unique continuous pattern. In most cases, they serve a dual purpose of protecting the internal organs from physical damage, and at the same time, enable in facilitating inter-cellular activities and prevent pathogen break ins. While the tissue mechanics and its proliferation have been scrutinized to great detail, it is their geometric uniqueness, that has remained more or less unexplored. With an intent of doing the same, this thesis identifies and explores those geometric properties/parameters that have an influence on the micro structure's homogenized and localized response. However, it does so by extracting the microstructures profile and representing its cell edges via three dimensional beam elements - hence the name, bio-inspired structures. The analysis is carried out by first developing a staggered Representative Volume Element (RVE) using finite elements, and identifying its appropriate size. The staggered assembly aids in minimizing boundary effects from creeping in, and at the same time, provides the requisite statistical homogeneity. This is followed by the geometry study. A wide range of epithelial geometries are considered for the study, ranging from completely isotropic skin models, to in plane anisotropic cuboidal structures and out of plane anisotropic stratified geometries. The effects of orientation, relative density and edge length are extracted and studied in great detail. It is observed that cell edges initial orientation has a direct dependence on the particle distribution, whereas the change in orientation is largely dependent on the deformation the microstructure is subjected to. Relative density is documented to show a direct correlation to a materials homogenized response i.e. larger the relative density, greater is the microstructures stiffness and homogenized stress response to the same deformation. Edge length, on the other hand is observed to showcase a downward trend on the cell edge's axial stress. On average, in any kind of distribution and any kind of deformation, smaller cell edges are known to showcase larger stresses, as compared to the larger cell edges.

# 1. INTRODUCTION

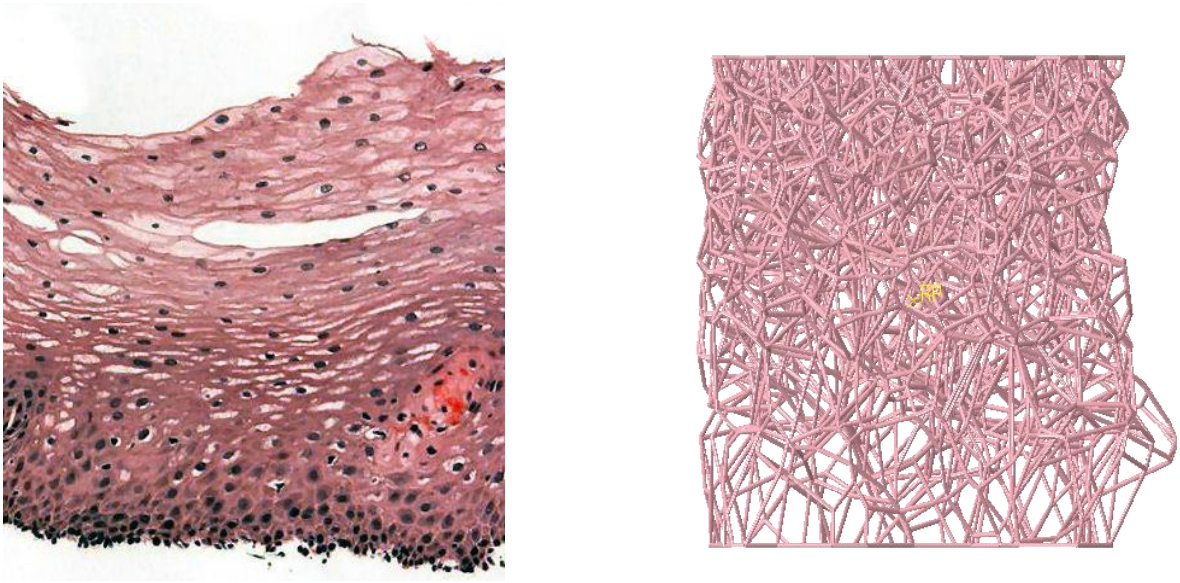

**Figure 1.1.** A side by side comparison of the stratified epithelial tissue structure found in esophagus with the stratified open-foam cell edge microstructure [1]

Biological systems, such as epithelial tissues are known to exhibit very unique microstructure geometry and cell arrangement [2]. As a result, these patterns have fascinated a wide range of scientists and engineers of every era - from Robert Hooke attempting to peek through a wine cork with his medieval microscope, to microbiologists and scientists trying to model cell growth and proliferation in skin tissues to engineers and designers attempting to mimic and develop structurally alike mechanical systems and mechanisms [3]–[5]. Now, what is truly fascinating about these structures is the geometric uniqueness they showcase, as they span and engulf an eclectic range of three dimensional sub-spaces [6]–[8]. Simple cuboidal cells found in the inner linings of the stomach and the intestines, although randomly distributed in its corresponding hyper-plane, are single layered, and their cells are columnar in shape[9]. Keratinized skin tissue on the other hand, observe a stratified distribution of cells along their thickness i.e. the size of the cell reduces as you go from the base of the tissue to the outer surface[10]. Going through the vast histological data of epithelial tissues makes

you question the very influence of these geometric properties on its homogenized mechanical response i.e what are these properties, and how to do they affect their response.

This question is actually derived/inspired/stems from a more prominent one i.e. to understand why epithelial tissues behave the way they do. This has been proven important for a multitude of reasons, and as a consequence, has been addressed in a plethora of ways. A prominent approach to this question would start by understanding the role of epithelial tissues. Epithelial tissue, as we know it, constitutes the largest organ in our body, covering vast expanses of both, outer and inner surfaces[11]. It is primarily responsible for protecting delicate organs, not only from zombies in the outer world, but also from pathogens and harmful chemical reactions that can disrupt the physiological processes and activities of the neighbouring cells. Common examples of physical protection include - 1) Any violent crash that might result in the rupturing of an organ/s, 2) Subjection of extreme temperature changes, which might be a result of a fire or some chemical reaction. In such scenarios, understanding the mechanical behavior of tissue structure becomes paramount, as it directly helps in the treatment of tears and burns. For instance, the study of tissue mechanics has played a prominent role in making complicated surgical procedures possible [12]–[14]. It is the experimental work of stretching skin samples and fitting their homogenized response to material models, that has enabled the computation domain to model tissue structures effortlessly [15]–[18]. Several researchers have thus been able to simulate these surgical procedures using Finite Element softwares and advise surgeons on more suitable techniques based on parameters like skin deformations and stress concentrations. While this approach addresses tissue mechanics very well, it does not allow you to extend its scope to our first question i.e. how is the tissue's microstructure contributing to that response? An insight on how the tissue microstructure looks like, and how it translates to the stress distribution developed within it remains unanswered.

A second common approach to understanding epithelial tissue response arises from biological curiosity. Tissue monolayers are known to exhibit mechanical stresses in morphological processes like mitosis, cell motility and delamination [7], [19]–[21]. In this regard, you observe extensive research in developing and applying numerical models that accurately capture cell sheet dynamics of such systems. Vertex dynamic models, as they are called, are prominently

used to investigate both elastic, viscoelastic and plastic behavior of such systems[22]–[24]. Consequently, there are some papers that focus on identifying and highlighting the biological parameters like contractility of actin-myosin rings and molecular adhesion, and their effect on mechanical response[25]–[27]. They also provide a great insight on the contribution of geometric extension of cell and cell division to the same response[28]–[30]. While biological papers with this approach certainly discuss one of the important properties of such microstructures i.e. orientation, the analogy is limited to just that i.e. they do not investigate the effect of relative density, connectivity, and/or any other localized properties that might also have an impact. Moreover, the study is limited to two dimensions i.e. monolayers. This means that the work does not indulge into anisotropy, not just in the plane, but also out of plane i.e. into the thickness of such tissues. There is, thus an inherent need to understand the role of the same geometric properties in all sorts of patterns and geometries.

There are good histological papers that clearly showcase the range of geometries seen in an epithelial tissue structure[9], [10], [31], [32]. There has also been a general need to understand the effects of these parameters with an aim of furthering of knowledge in that domain.

In this thesis, we list and classify these geometric parameters and study their effects on the homogenized response of common epithelial tissues. This includes tissues which showcase anisotropic distribution of cell particles within the plane, and out of plane. We also investigate how these geometric parameters might have an influence on the stress distribution within each cell. The detailed process flow is provided here. Chapter 2 comprises of a detailed methodology on how the microstructure geometry is constructed. It starts by emphasizing a great deal on how the distribution of cells within the geometry influences the microstructure. The geometry in itself is conceived by the principles of voronoi spaces, where each particle represents a voronoi cell, and its vertices, a collection of points closest to the subspace in question. The connection of such points in a pre-determined sequential order can be visualized as cell edges, which together form the overall microstructure about the particles. Each particle is assumed to have the same weight associated. As a result, we propose an open foam vertex connected beam structure in our thesis. The decision to develop an open foamed structure as opposed to closed foam geometry, is because we are purely interested in

studying just the geometric effects and not necessarily in capturing the actual behavior of such tissues. In order to do so, one would need to account for all the biological phenomena that occur during mechanical stretch i.e. develop an extension to the active vertex model to three dimensions, and , at the same time, incorporate and investigate the geometric effects. This methodology unnecessarily complicates the process, rendering the direction mute. As a result, to characterize the structure of a cell, we make an assumption that cell edges can be represented by three dimensional beam elements. By doing so, we are able to preserve the geometric characteristics of epithelial tissues. Now, it is important to remember the fact that the consequence of doing so, results in a epithelial tissue like structure, similar in geometry, but different in composition. Hence the name, epithelial tissue-inspired structures. Geometry creation is followed by the application and need for creating periodic geometries in next sub section. Since the geometry in question is intended to span the entire subspace, developing a repeating structure makes sense. To extract the complete three dimensional response of the geometry, we propose three distinct biaxial stretch simulations. The methodology of extracting the homogenized response of the structures is explained in the final sub section.

Chapter 3 focuses entirely on the development of a Representative Volume Element (RVE), with the discussion flowing from the methodology and size determination, to performing and analyzing the homogenized response of every RVE size. The final chapter includes all the variations of the geometric properties, and the study of their homogenized response. Cell edge orientation, relative density and the localized response of a completely isotropic material is studied first. This is followed by the anisotropy study of commonly observed epithelial tissue structures. The thesis ends by summarizing the contribution and effects of the geometric parameters on epithelial tissue-inspired structures, and overlays the future work that can take this research forward.

# 2. MATERIALS AND METHODS

## 2.1 Geometry Creation: From Voro++ to ABAQUS

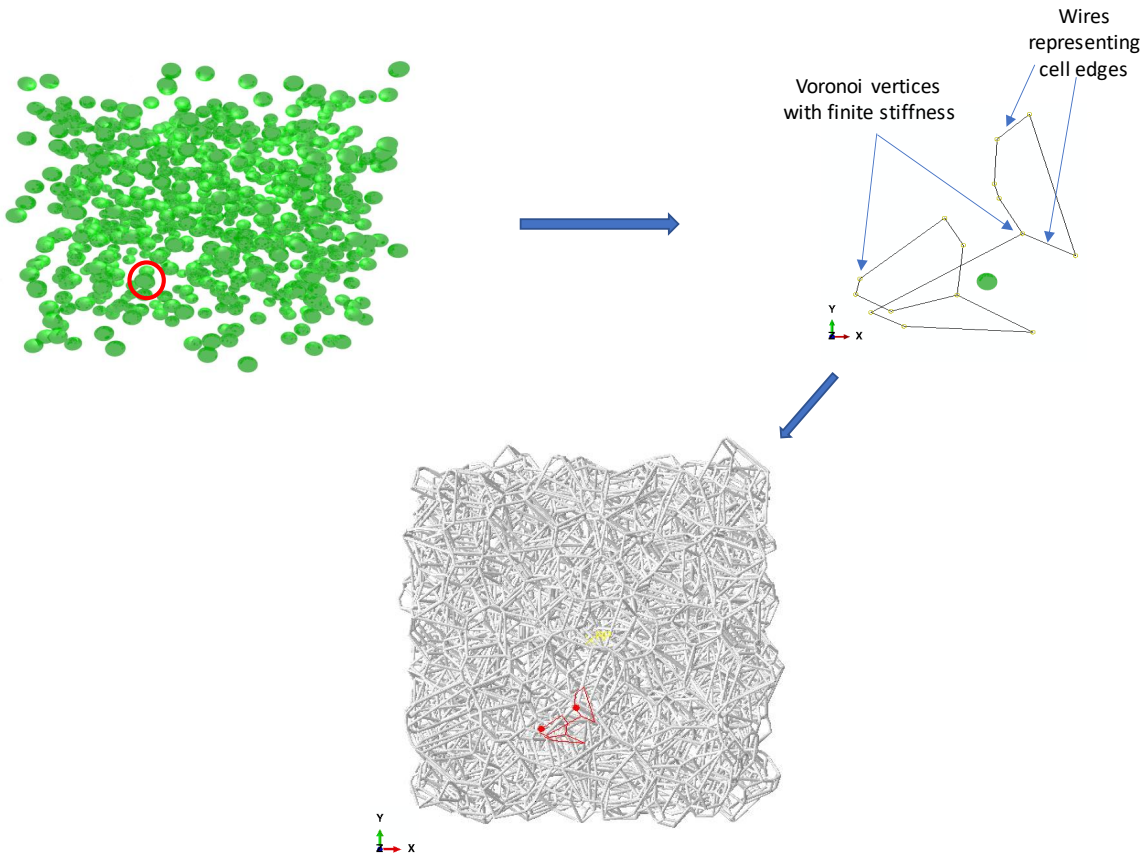


**Figure 2.1.** The geometry creation flowchart for all microstructures: Voro++ assists in converting the particle distribution in 3D space into voronoi sub spaces. The resultant geometry is imported into co-ordinates of con-jointed poly-lines, which are in turn scripted into ABAQUS as cell edges with finite stiffness. The combination of all poly lines results in the overall voronoi tessellation.

The process of developing the tissue microstructure begins with the creation of the geometry in Voro++[33]. Histologically accurate cell density and distribution of the tissue is fed into the software, along with its size and output post processed data requirements. Upon receiving this data, a computationally accurate voronoi tessellation is generated that spans the domain space. Now, it is well understood that developing a model of the entire

tissue is not necessary - only a statistically periodic representative volume element that can be tiled repeatedly in the hyper-plane does the job well. A geometry, periodic in x and y and non periodic in z is thus developed. The methodology of experimenting and deciding the true RVE size is explained in the next chapter. The same process is repeated for all microstructures and cell distributions showcased in this thesis.

The geometry, consisting of several con-jointed poly-lines, is first visually analyzed in a POV generator and then imported and scripted in the Finite Element software, ABAQUS via Python[34]. The output geometry is entirely represented by wires, which when connected together in a sequential pattern constitute the overall geometry. The wires signify the edges of a voroni cell and are intended to capture the deformation behavior of the structure. Thus, scripting/connecting all the individual poly-lines together with joints of finite stiffness will ultimately yield the voronoi tessellation in the Abaqus environment. At this stage, a majority of the geometric properties are already assigned - particle distribution, wire orientation and vertex connectivity. Once the model is generated, the next step that is assigning the last two crucial properties that will define its behavior - material properties and beam profile radius. To mimic the elastic behavior of tissue microstructure, the following strain energy density function is adopted -

$$\Psi = C_{10}(\bar{I}_1 - 3) + \frac{1}{D_1}(J-1)^2, \tag{2.1}$$

where the material constants are represented by $C_{10} = \mu_0/2 = 0.83$ kPa and $D_1 = 1/\text{K} = 0.0612$ kPa and the strain state is given by $I_1$ and J. In the expression, $\mu_0$ represents the shear modulus of the material, and K represents the bulk modulus. Their corresponding values are obtained by referring to the experimental studies performed on similar tissues in the literature [35], [36]. The need for a nearly incompressible model, arises to address the computational difficulty faced in such problems. Non linear simulations such as these are known to encounter convergence issues when they deal with purely incompressible materials. Thus, to counter that, a very small compressibility factor is iterated and utilized here [37].

It has been well established in previous literary work that deformation seen in open foam structures, when subjected to external loads, are more accurately captured with three di-

mensional flexible beams, than trusses[6], [38]–[41]. This is because each wire, as a result of the nature of the connectivity is subjected to not only axial but also a combination of in-plane and out of plane shear forces and concentrated moments. And this is a result of the elastic nature of the vertex joints - they possess a finite stiffness, thereby resisting the rotation of the joint about all three axes, thereby declaring a beam element as an ideal choice. With this analogy, each wire is modelled with a shear deformable three dimensional two node beam element. A non-linear hybrid B31-H Timoshenko beam element is chosen for this purpose. It has been shown in past literary work that hybrid elements work best for close to incompressible material models and hence the choice [37]. While the beams are intended to capture the mechanics of deformation during stretch, there are no contacts defined/established between them. This underlying reason is given here - we intend on capturing the geometric properties of open foam structures and their influence on deformation. Including contact properties complicates the problem unnecessarily. Deciding the element choice now introduces the final parameter that represents the model geometry - beam profile radius. It is influenced by two constraints - 1) Aspect ratio of the wire, and, 2) Average relative density of the model. Aspect ratio of a B31-H beam element is known to capture deformation accurately unto a value of 1/5 [42], [43]. Anything beyond that, will introduce errors into the simulation, and the structure should no longer be modelled using beams, but rather by a solid three dimensional element.

The final constraint influencing beam profile radius is the relative density of the model. Literature defines a cellular solid as that microstructure whose relative density is less than thirty percent [38]. Anything greater than that, is usually considered as a transition solid and is thus not modelled using this methodology. With these two constraints, an appropriate profile radius is chosen, satisfying both the parameters. The model, at this point is ready to be subjected to multiple loading conditions and deformations.

### 2.2 Tiling the hyper-plane: creating periodic boundaries

The reasoning behind developing periodic boundaries for the model is two-fold - 1) It is crucial to develop a microstructure that when tiled repeatedly in x and y, spans the entire

two dimensional sub-space, and, 2) Periodic boundary surfaces, as opposed plane square surfaces, eliminate the presence of straight and perpendicular bounding edges, something that is nonphysical and unheard of in regular tissue microstructures. Even though the former condition of two dimensional space tiling is met by square bounded geometries, the introduction of the bounding edges lead to unusual and restricted deformations, something that does not occur in tissues. This analogy, however, does not hold true to the third dimension of thickness, as the model is not meant to span in z.

### 2.3 Applying boundary conditions to Finite Element Model (FEM)

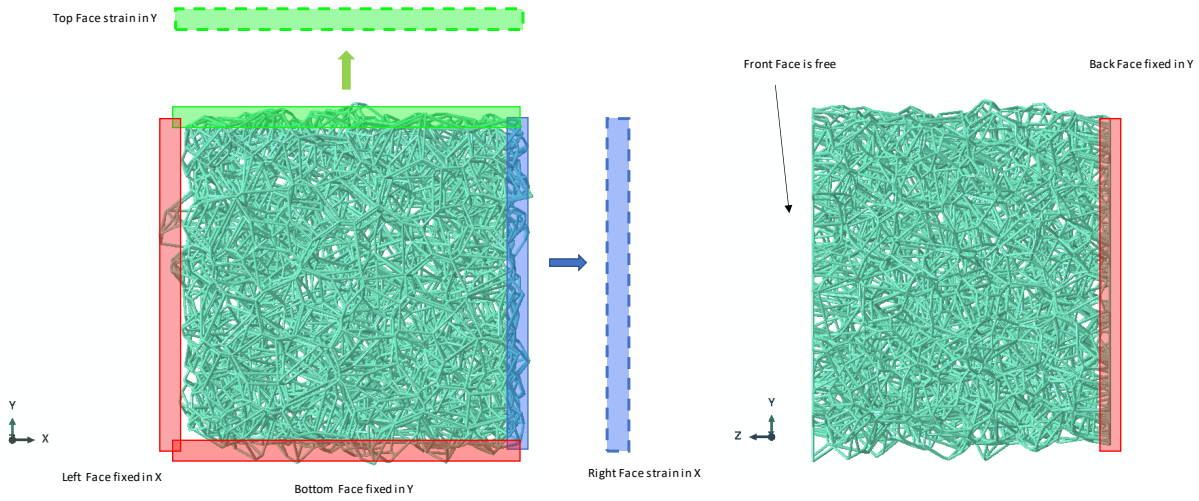


**Figure 2.2.** Boundary conditions: Cell edges passing through three faces i.e. Left Face, Bottom Face, and Back Face are fixed in x, y and z directions respectively. Cell edges passing through Right and Top Faces have displacement boundaries specified. The Front is free from any boundaries.

The model is subjected to in-plane displacement boundary conditions, satisfying the need to mimic typical deformations of epithelial tissues [18], [44], [45]. It is subjected to three classical tests - 1) Equi-Biaxial stretch in x and y, 2) Off-Biaxial stretch in x, and, 3)Off-Biaxial stretch in y, each satisfying an inherent need to understand the non linear tissue response [46]. This process is carried out by establishing displacement strain on the first five distinct faces of the geometry and leaving the sixth face, free of constraints (surface of

the tissue). From the figure shown above, the right and top face is subjected a non zero tensile strain about their respective perpendicular axes. In the meantime, the left and the bottom face is restricted from any strain in the same axis. The back face is fixed in z, while the front face is free from all boundary conditions. Now, in an ideal sense, one would be in favour of applying periodic boundary conditions to opposing faces - this process eliminates any boundary effects that can creep in through the edges and allows the geometry to deform as though the entire plan is spanned by it. However, attempting to do so on the requisite geometry leads us to a new computation problem - opposing boundary faces of the model no longer have the same profile, which in turn, entails that the opposing faces no longer have equal number of nodes. Periodic boundary conditions cannot be used for such geometries [47]. To circumvent this situation, a new method is proposed - the response of the geometry will be measured, not from the boundary, but rather, from an inner RVE that lies within the bounding region. The size of this region, along with the size of the RVE box will be determined appropriately so as to minimize any boundary effects that might creep into the model.

### 2.4 FEM Post-processing: Obtaining homogenized response

To characterize and define the homogenized response of the deformation, we need to establish a methodology of quantifying the stress and strain response of the whole model. To do so, we generate an arbitrary fictitious plane that passes through the geometry entirely and is perpendicular to one of the cartesian-coordinate axis. After doing so, we take an account of all the elements passing through the plane, and calculate their internal elemental stress S11. One thing to remember at this step, is that the internal stress developed is given in the deformed configuration i.e. it is the force per deformed beam cross sectional area. Taking this into account, we extract the appropriate internal force developed within the beam element, and, subsequently the contribution of the elemental force to the response along the

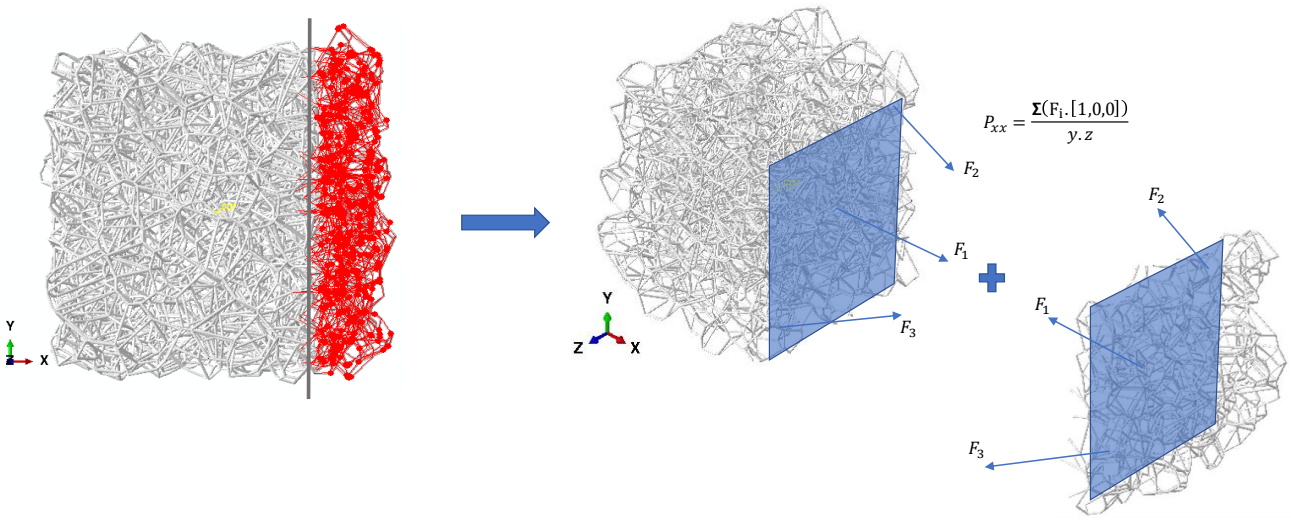


**Figure 2.3.** The methodology of extracting the homogenized stress and strain response - creating a fictitious plane passing through the geometry, and accounting for the intersecting cell edges and their response

co-ordinate axis in question, using the following equation. This equation is summarized as follows -

$$
\begin{aligned}
P_{xx} &= \frac{\sum_{\text{i}}^{\text{All intersecting cell edges}} (F_{\text{i}}.[1,0,0])}{\text{Undeformed plane area y.z}}, \\
P_{yy} &= \frac{\sum_{\text{i}}^{\text{All intersecting cell edges}} (F_{\text{i}}.[0,1,0])}{\text{Undeformed plane area x.z}}, \\
P_{zz} &= \frac{\sum_{\text{i}}^{\text{All intersecting cell edges}} (F_{\text{i}}.[0,0,1])}{\text{Undeformed plane area x.y}},
\end{aligned}
\tag{2.2}
$$

Summing the contribution of internal forces of all intersecting elements and dividing it over the un-deformed plane cross section area gives us the expression for the homogenized first Piola-Kirchhoff stress at the plane. Performing the same across the remaining two cross sections gives us the response in y and z axes. Now, our methodology of extracting the

homogenized response of the microstructure makes use of just the axial forces in the beam, and not the components responsible for torsion/twist in the member. This assumption can be made in our case, as the internal reaction moments responsible for twist turns out to be significantly small. As a result, the resulting internal torsional stresses generated in individual elements are significantly small, and are ignored.

The true strain of the plane in question, can be obtained by calculating the average displacement response of all the intersecting beams. This analogy, although accurate, does contain the boundary effects. To try and mimic a true periodic boundary, similar calculations are performed on an opposing face (equi-distant from the center-plane of the geometry), and the two are subtracted as follows. This technique is intended to separate any displacement that might've taken place within the geometry, from the true strain that the model is subjected to. By doing so, the post-processing technique is ready, and the homogenized response of any Inner geometry within the structure can be extracted and calculated.

# 3. REPRESENTATIVE VOLUME ELEMENT STUDY (RVE)

## 3.1 Size determination: Criteria

The need for a representative volume element becomes paramount, especially when one is dealing with microstructure geometries that are intended to span vast spaces[48]. In such scenarios, modelling entire geometries is not only computational tedious and expensive, but also highly inconvenient. With this foundation, an appropriate RVE is explored i.e. the one that not only captures the statistical homogeneity of epithelial tissues, but is, at the same time, small enough to make computation feasible. What that means, is that the suggested size should be large enough that the model alone contains all the necessary quirks that a randomly selected model would. It should essentially capture the same orientation distribution, contain the same relative density, volume fraction, and should have sufficient lapses that a generic sample would[49]. With this analogy, we know that anything lager than the minimum size would work just fine. However, to make the study computationally viable, it is important that we recognize the threshold size.

Having established the need for an RVE, the next step is to estimate the appropriate size of it. In a classical method, one would usually be concerned only about parameterizing the outer size of the RVE. However, in our case, the need to eliminate boundary conditions creates a second parameter that needs to be optimized i.e. deciding the geometric dimensions of the inner region, which we will now refer to as the Inner RVE. From a mathematical perspective, we will need to maximize the inner RVE geometry and minimize the ratio between the Inner RVE and the outer box for the following reasons -

1. To ensure that all the necessary statistical homogeneity is captured, and
2. To eliminate boundary effects.

Satisfying both the conditions will ultimately help decide the appropriate Inner RVE and Box dimension. Now, the first parameter is crucial when dealing with experimental samples which usually possess impurities in the form of voids and inclusions in their systems [50]. Including sufficient material in the RVE becomes paramount, as you are not strictly in control of the distribution of the said impurities. In our case, however, it is us, who

decide the distribution of the particles i.e. we decide the cell distribution. Now, it is true that random structures might introduce some variation in the results. However, it is still manageable, compared to the second parameter. In an ideal geometry, cutting the geometry and calculating the resultant reaction forces at any plane should be essentially the same. As we learn in basic mechanics, it should be independent of the position of the cut. However, our study tells another tale. Thus, identifying and minimizing this factor becomes of prime importance in this study. The entire chapter, thus focuses on that.

To start with, three arbitrary box sizes are chosen, and at the same time, three arbitrary inner RVE sizes are chosen. The average RVE thickness A combination of the two parameters is going to yield nine different configurations of the setup, as shown in the figure. The specifications of the three boxes and Inner RVE sizes are all provided are listed below:

1. Configuration 1,2,3: Inner RVE 1: 30 $\mu$m x 30 $\mu$m x 75 $\mu$m (l x w x h)
   (a) Box 1: 50 $\mu$m x 50 $\mu$m x 75 $\mu$m
   (b) Box 2: 75 $\mu$m x 75 $\mu$m x 75 $\mu$m
   (c) Box 3: 100 $\mu$m x 100 $\mu$m x 75 $\mu$m
2. Configuration 4,5,6: Inner RVE 2: 40 $\mu$m x 40 $\mu$m x 75 $\mu$m (l x w x h)
   (a) Box 1: 50 $\mu$m x 50 $\mu$m x 75 $\mu$m
   (b) Box 2: 75 $\mu$m x 75 $\mu$m x 75 $\mu$m
   (c) Box 3: 100 $\mu$m x 100 $\mu$m x 75 $\mu$m
3. Configuration 7,8,9: Inner RVE 3: 50 $\mu$m x 50 $\mu$m x 75 $\mu$m (l x w x h)
   (a) Box 1: 50 $\mu$m x 50 $\mu$m x 75 $\mu$m
   (b) Box 2: 75 $\mu$m x 75 $\mu$m x 75 $\mu$m
   (c) Box 3: 100 $\mu$m x 100 $\mu$m x 75 $\mu$m

The in-plane dimensions of both the Inner RVE and the Box are chosen arbitrarily, whereas the thickness is established from the existing literature. This is because the geometry

is in fact, not tiled along its thickness i.e. in the z direction, and hence needs no alteration. Thus, for an epithelial tissue sample taken from the dorsal portion of the palm, the overall thickness of the epithelial tissue structure can be assumed to be $75\mu$ m [10]. Now, it can be concluded from the list that the second parameter i.e. size ratio between the two sizes will range from a minimum of 0.3 to a maximum of 1, with the box three and Inner RVE one having the smallest size ratio, to box one and Inner RVE three having the largest size ratio of one, respectively.

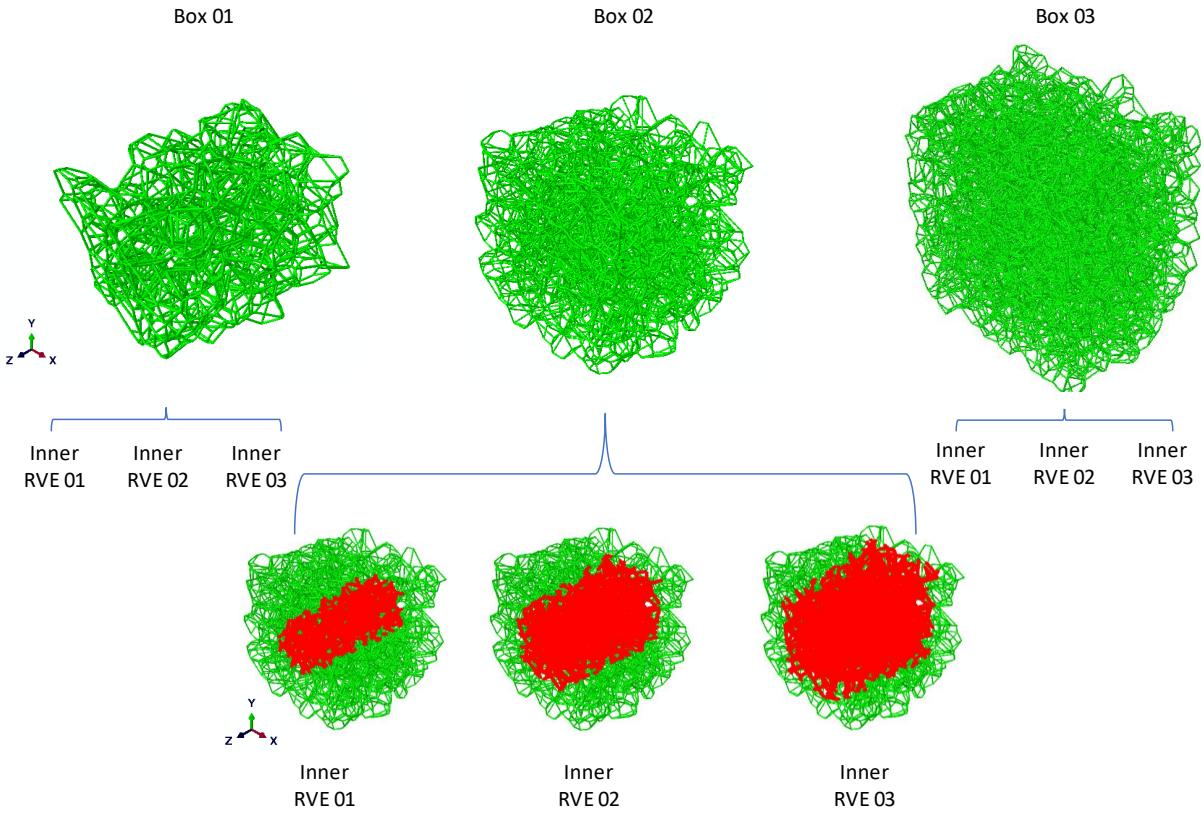


**Figure 3.1.** Configuration setup for all the Inner RVE's and boxes. Each Box size variation comprises of three inner RVE variations i.e. in total 9 configurations. Each configuration has a total of 5 samples each, to account for randomness in the microstructure geometry.

The point of obtaining reliable and consistent results is often raised in such simulations. Since the geometries obtained are assumed to be completely random, there is a possibility for every model to possess an inherent bias/anisotropy within itself. Thus, to address this point, five samples for each box configuration is generated. This ultimately eliminates any variance/bias that might've been introduced into the system and, at the same time, provides confidence in the results[48]. Thus, with the suggested range of RVE dimensions, the respective model samples are generated, and their corresponding homogenized response for the models are plotted and analyzed.

The methodology of analyzing both Inner RVE size and the size ratio adheres to the following analogy - It is of utmost importance to first define the validity of the data being scrutinized. If the data in question is not consistent, we cannot definitively place any confidence in it. To enforce this, we incorporate five samples into the mix and observe the variance of their homogenized stress strain response at a strain of 10 percent. If the variance in data is greater than a certain threshold i.e. user defined 15 percent, the samples are deemed unfit for analysis and new samples for the same configuration are generated. The process is repeated until this criteria is met. The methodology adopted, is similar to paper [48], which also showcases similar means of ensuring consistency in results.

In our data, you can clearly observe from the table that all nine configurations have achieved the set variance when subjected to all three loading conditions and tests. This data is now set to be analyzed further, to optimize the two governing parameters for the RVE study. The same can be concurred by observing the variance plot provided in figure xx.

Iterating through multiple model geometries helps us identify the perfect samples that satisfy statistically similar model geometries. Once this is ensured, we delve into identifying the appropriate RVE size. The proposed process flow for deciding the correct configuration is going to be the following:

This study provides a comprehensive review and comparison between the nine configurations discussed earlier.

1. Pick the configuration 1 i.e. smallest inner RVE and smallest Inner RVE to box ratio i.e. Inner RVE 1 and Box 1

2. Obtain the homogenized stress response in both x and y at a strain of 10 percent. Do the same for all three tests (Equi-BI, Off-X and Off-Y).

3. Pick the next configuration i.e. 2, same Inner RVE, but Box size 2

4. Obtain its corresponding homogenized response in the plane at the same strain.

5. Now, estimate the relative error that exists between the two consecutive configurations.

6. Repeat the process by looping through the remaining seven configurations and obtain the homogenized response and their corresponding relative errors.

## 3.2 RVE study: Homogenized response

The homogenized stress strain response for all configurations and samples have been plotted in Fig. 3.2. Subsequently, their stress response in the plane at a strain of 10 percent has been tabulated in Fig. 3.3, along with the relative error that exists between box 2 and 3 for all the three Inner RVE configurations. The blue plot consists the interpolated data for the homogenized response for the first box configuration. The green plot provides the response for the second box, whereas the red plot provides for the last i.e. third box configuration.

### 3.2.1 Configuration 1,2,3: Inner RVE 1 - Box 1,2,3

The Equi biaxial plot for Inner RVE 1 (Row 1, Column 1) provides the homogenized stress strain response in x and y for all three box configurations. In it, we make the following observations:

- The stress response in both x and y appear to coalesce, for every Inner RVE - box configuration i.e. visually speaking, there is little to no variation. This indicates that the microstructure in question is truly isotropic in nature, in it, that it showcases similar mechanical behavior in the plane. The same can be inferred quantitatively by comparing the stress response in x and y from Fig. 3.3. On average, you observe a

variation of at-most, 5 percent. This is a good indication that the microstructure is in fact, isotropic in nature.

- The statistical variation between samples for each configuration is well below the threshold limit, throughout the strain range. The variance for Box 1 and 2 turn out to be very low, which conclusively proves that a statistical mean is achieved. However, the variance for box 3 is considerably higher. This is because of the lack of sufficient data points for larger strains - box 3 is the largest structure of the three, could not achieve high strains, as box 1 or 2 did, citing divergence issues in the simulations.

- Boundary effects can be clearly seen creeping into the box 1 configuration as its response seem to be way off as compared to Box 2 and 3. However, the same is not true for the next configuration i.e. 2, as the response between Box 2 and 3 is very similar. This is proven true after observing that the relative error between the configurations is 6 and 11 percent in x and y respectively Fig. 3.3. This study showcases the fact that by switching the size of the outer box, we are able to reduce the Inner RVE to box ratio, thereby eliminating boundary effects. Once this condition is achieved, any further reduction of the size ratio has little to impact on the homogenized response, as can be inferred by the relative errors.

Observing the remaining two plots in the row gives an overview on off biaxial deformations:

- It is observed that the variation of stress response within the plane remains very low for both off biaxial stretches. This is a good indicator that, irrespective of the displacement boundary conditions, the model is subjected to, the model experiences similar stresses in the plane, rendering the model truly isotropic. We can thus conclude that the random distribution of particles in the medium does result in a isotropic microstructure.

- For a particular strain, the stress observed in any of the off biaxial deformation is lower than its response in the equi biaxial test.

- Box 1 shows clear presence of boundary effects, as you observe a sudden jump in stress as the configuration is moved to box 2. The same is not true for the change in configuration from box 2 to 3 - the stresses, in fact, are very similar in magnitude, and showcase low relative error in their response in both x and y. One thing to notice though, is that only the Off-Y deformation follows the norm (relative error of 11 and 13 percent), while there is a significant deviation of stress levels for the Off-X data with a relative error of 32 percent in x. The response in y is reasonable with a relative error of 6 percent. Thus, this might be an anomaly.

The analysis of all three configurations of Inner RVE conclusively proves that the relative error for configuration 2 i.e. Inner RVE 1 - Box 2, showcases a relative error that is below our accepted norm of 15 percent. This configuration, has thus been able to minimize the boundary effects from creeping in. From this analysis, it is clear that we can proceed with the rest of the study with our choice of RVE. Anything larger will only increase the extent of boundary effects creeping in, and will hence be a less desirable choice. However, for the sake of completeness, we showcase the same by analyzing configurations 4 through 9 in the next two sections.

### 3.2.2 Configuration 4,5,6: Inner RVE 2 - Box 1,2,3

The analysis of Configurations 4 through 6 also showcase promising results. As we go through all the three deformation types, we observe box 2 to showcase almost consistent results with box 3, with relative errors still being in the acceptable range for most of them. It is the off biaxial stretch in x, that continues to showcase irregular stress response in x. The reason why that occurs might be purely statistical, as we might have one of the simulations going rogue by attaining instabilities.

### 3.2.3 Configuration 7,8,9: Inner RVE 3 - Box 1,2,3

Moving to the third and final Inner RVE size, raises some intriguing questions. Starting with configuration one, we observe that the stress response for the 7th configuration i.e. box 1, is close to zero. Here, the size of the Inner RVE is same as that of the box. We believe

this is due to the presence of our fictitious plane being so close to the boundary. All the edges, under the influence of the free end of the boundary, experience little to no resistance to displacement. As a results, their internal stresses are close to zero. Configuration 8 on the other hand, does not fair any better either, as the Inner RVE to box ratio has risen significantly. Citing no reason to proceed the analysis further, we abandon ship, and move forward with our research with the previously accepted configuration i.e. 2 - Inner RVE 1 - Box 2.

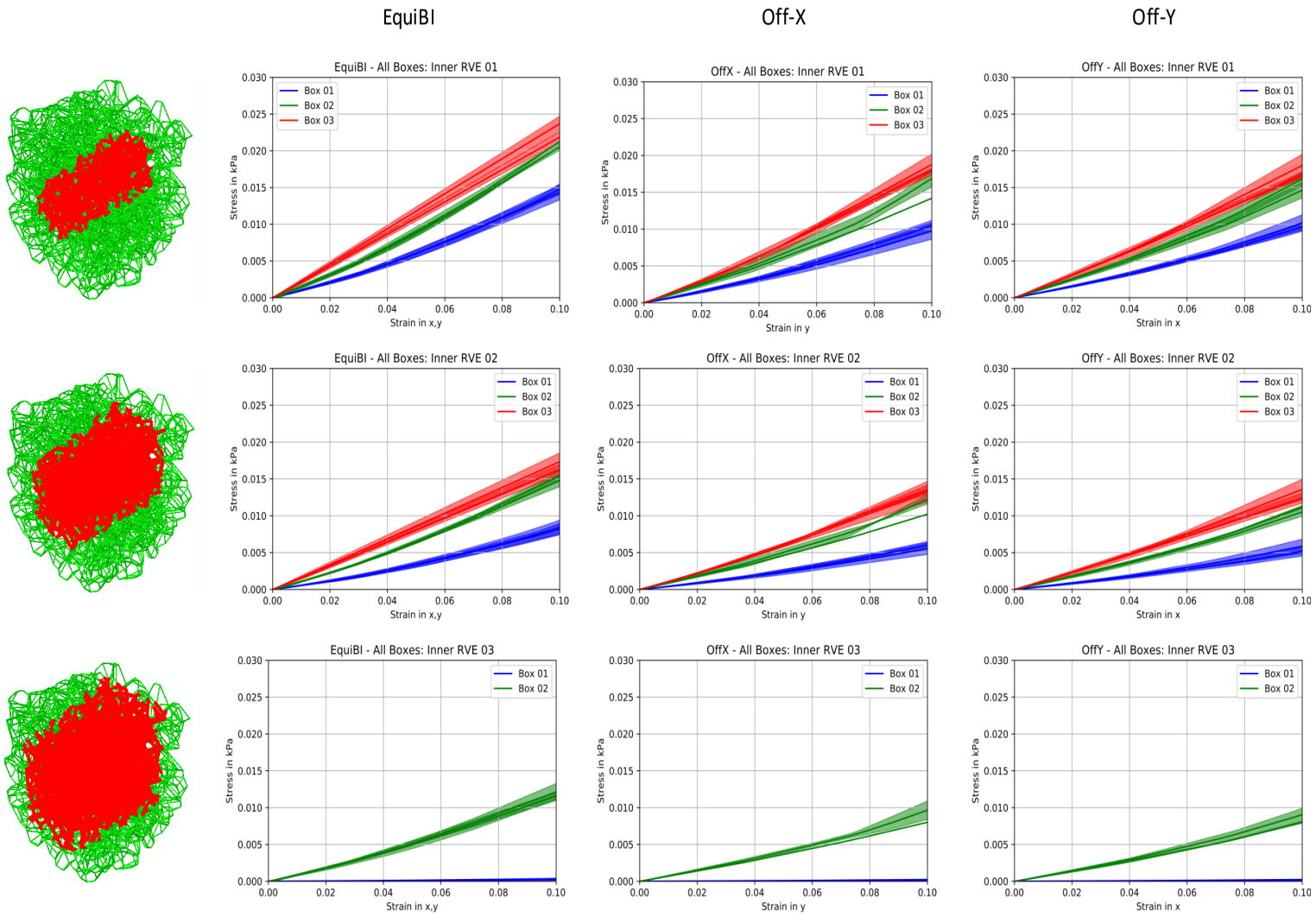


**Figure 3.2.** RVE Study: Homogenized response of the RVE when subjected to in plane deformations. Comprises of interpolated simulation data.The mean is represented by a solid line and the variance of 5 samples with the shaded curve. First row - Inner RVE 1's Stress-Strain response for all three box sizes. Consequently, the second row - Inner RVE 2's Stress-Strain response for all three box sizes, and the third row - Inner RVE 3's Stress-Strain response for all three box sizes.

| STRESS RESPONSE IN X (kPa) @ 10% STRAIN | | BOX 1 | BOX 2 | BOX 3 | RELATIVE ERROR (BOX 2 AND 3) |
|---|---|---|---|---|---|
| EQUI-BI | RVE 1 | 0.014325 | 0.0205307 | 0.021843 | 6.391891168 |
| | RVE 2 | 0.00842483 | 0.0147753 | 0.0162577 | 10.03296041 |
| | RVE 3 | 0.000209707 | 0.0116065 | 0 | NA |
| OFF-X | RVE 1 | 0.00997809 | 0.0145221 | 0.0191806 | 32.07869385 |
| | RVE 2 | 0.00567913 | 0.0104488 | 0.0135757 | 29.92592451 |
| | RVE 3 | 0.000152789 | 0.00819183 | 0 | NA |
| OFF-Y | RVE 1 | 0.0101732 | 0.0161641 | 0.0179935 | 11.31767312 |
| | RVE 2 | 0.00585289 | 0.0111986 | 0.0127916 | 14.22499241 |
| | RVE 3 | 0.000131901 | 0.0090389 | 0 | NA |

| STRESS RESPONSE IN Y (kPa) @ 10% STRAIN | | BOX 1 | BOX 2 | BOX 3 | RELATIVE ERROR (BOX 2 AND 3) |
|---|---|---|---|---|---|
| EQUI-BI | RVE 1 | 0.0147726 | 0.0212331 | 0.0236778 | 11.51362731 |
| | RVE 2 | 0.00824093 | 0.0154198 | 0.0173289 | 12.38083503 |
| | RVE 3 | 0.000327239 | 0.0121192 | 0 | NA |
| OFF-X | RVE 1 | 0.0104817 | 0.0168713 | 0.0180175 | 6.793785897 |
| | RVE 2 | 0.00599031 | 0.0122651 | 0.0135615 | 10.56982821 |
| | RVE 3 | 0.000211549 | 0.00964619 | 0 | NA |
| OFF-Y | RVE 1 | 0.00989252 | 0.0150105 | 0.0170437 | 13.54518504 |
| | RVE 2 | 0.00529171 | 0.0107791 | 0.0126512 | 17.3678693 |
| | RVE 3 | 0.000229884 | 0.008211 | 0 | NA |

**Figure 3.3.** A comparison of the homogenized stress response in both x and y at a strain of 10 percent, for all nine configurations, and for all three deformations. The final column provides the relative error between Box 2 and Box 3 for every Inner RVE.

| S.D IN X @ 10% STRAIN | | BOX 1 | BOX 2 | BOX 3 |
|---|---|---|---|---|
| EQUI-BI | RVE 1 | 0.000997752 | 0.000453959 | 0.000666811 |
| | RVE 2 | 0.000995919 | 0.00082993 | 0.000727211 |
| | RVE 3 | 8.11E-05 | 0.000497737 | 0 |
| OFF-X | RVE 1 | 0.00115087 | 0.000284204 | 0.00149622 |
| | RVE 2 | 0.000811794 | 0.000399083 | 0.00144071 |
| | RVE 3 | 7.40E-05 | 0.000610957 | 0 |
| OFF-Y | RVE 1 | 0.00112308 | 0.000974052 | 0.00154923 |
| | RVE 2 | 0.000966091 | 0.000214414 | 0.00138823 |
| | RVE 3 | 5.12E-05 | 0.000889052 | 0 |

| S.D IN Y (kPa) @ 10% STRAIN | | BOX 1 | BOX 2 | BOX 3 |
|---|---|---|---|---|
| EQUI-BI | RVE 1 | 0.000731435 | 8.47E-05 | 0.00104116 |
| | RVE 2 | 0.000724725 | 0.000694539 | 0.00120288 |
| | RVE 3 | 0.00010787 | 0.00115558 | 0 |
| OFF-X | RVE 1 | 0.000697227 | 0.00116316 | 0.000209992 |
| | RVE 2 | 0.000506102 | 0.000654702 | 0.000605239 |
| | RVE 3 | 7.67E-05 | 0.00125185 | 0 |
| OFF-Y | RVE 1 | 0.000449417 | 0.00110794 | 0.000422688 |
| | RVE 2 | 0.000657568 | 0.000604801 | 0.000705498 |
| | RVE 3 | 5.97E-05 | 0.000148489 | 0 |

**Figure 3.4.** A comparison of the Standard Deviation (S.D) of the homogenized stress response in both x and y at a strain of 10 percent, for all nine configurations, and for all three deformations.

# 4. RESULTS

Having identified an appropriate RVE size for the process, we can now delve into the analysis of geometric parameters and their influence on the RVE's homogenized response. Their influence on both the homogenized response and the localized stress distribution is thus investigated:

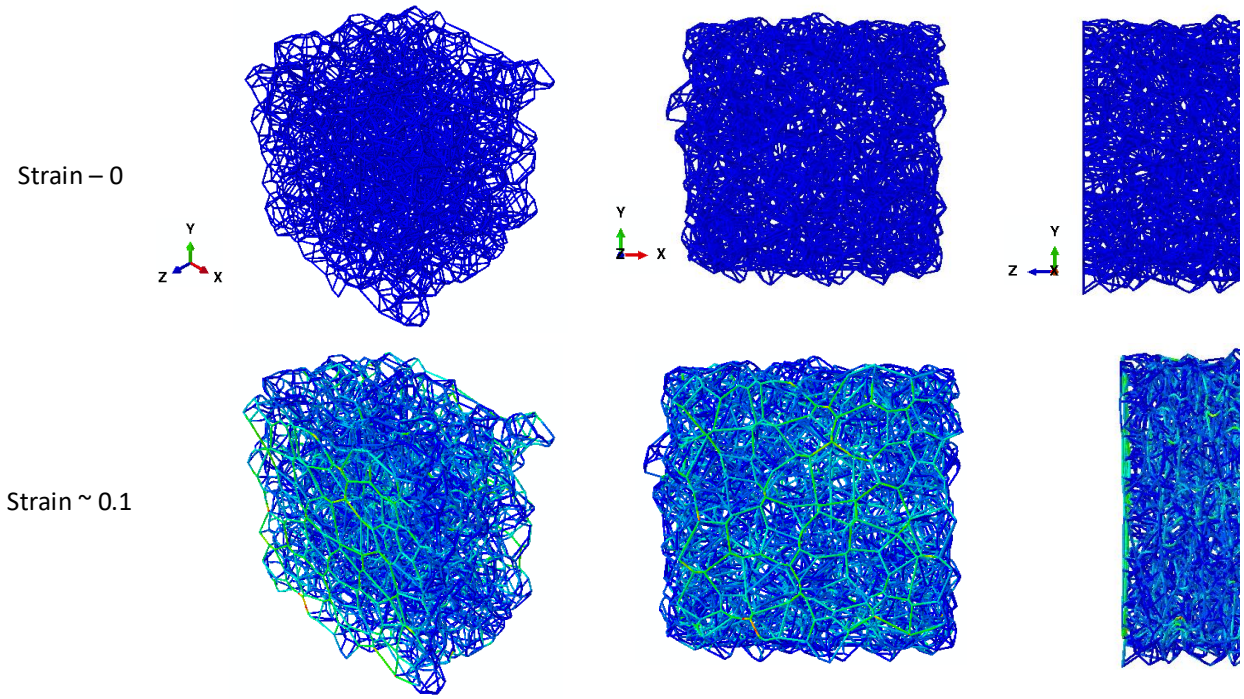


**Figure 4.1.** Uniformly random structure: First row - Isometric view, front view and side view at 0 strain. Second row - same views of the structure at approximately 10 percent strain. Third column showcases the advantage of using periodic boundaries in the hyper-plane - little to no boundary effects visible in the deformed structure.

## 4.1 Cell Edge Orientation

The first parameter we intend on investigating is the orientation of the cell edges and how it changes as the RVE is subjected to different strains. Any beam, in three dimensional

space can be represented uniquely as a combination of its direction cosines and the Cartesian normal's of the three dimensional space. We use this approach to identify our three orientation parameters i.e. alpha, beta and gamma. Alpha is the angle made by a cell edge with the positive x axis, beta is the angle made with the positive y axis and subsequently, gamma, with the positive z axis. These three angles together communicate the orientation of any cell edge and will hence be termed as the cell edge orientation parameters (see first column in Fig. 4.2. As the RVE is stretched to different strains, we track these parameters and develop their corresponding polar plots. The same is shown in Fig. 4.2 below, for three different loading conditions we earlier described.

The microstructure in the spotlight is the uniformly random RVE structure, which ultimately emerged as the appropriate model size. For a truly isotropic structure, we observe that the initial distribution of all three angles are uniform, which means that the statistical weight associated with every orientation is the same. Keeping this in mind, what one would expect would be a circular plot for all three orientation parameters. However, that is not observed in our figure, as we look at the blue dense polar plot for all deformations and orientation parameters. What you observe, is a mushroom kind of distribution of cell edges for all three angles, with the peak consisting of edges perpendicular to its associated co-ordinate axis. The observation of this particular phenomenon is particularly true, because of the nature of our co-ordinate axes, and the dimension of the sub space we deal with. For instance, an edge parallel to one co-ordinate axis is perpendicular to the other two. If you have three edges, each parallel to each co-ordinate axis, each orientation parameter will consist of two edges perpendicular to its own corresponding axis, and one being parallel to it, thus resulting in the gradient in the polar plot. If you account the same for an array of beams spanning the three dimensional space uniformly, the gradient you observed earlier morphs into the mushroom like distribution you see in our figure. Hence, the distribution is, in fact, perfectly represented by the initial polar plot for zero strain.

As the RVE attains a strain of approximately 10 percent, we observe that the edges tend to re-align themselves, in a somewhat biased fashion. The same can be concurred by taking a look at the overlapping hollow orange plots on the same figures as discussed above. Starting with the equi-biaxial stretch, we observe that the edges, as they deform, tend to

move toward the direction of stretch i.e. along x and y proportionally. The shift is seen because of the re-orientation of cell edges. This can be inferred by tracking the difference between the initial blue polar plot and the overlapped orange polar plot. You can clearly observe that the height of the mushroom profile tends to decrease in the alpha and beta plots, as the frequency of perpendicular beams drops. They are, in fact, re-orienting themselves along the direction of stretch. As a result, the alpha and beta plots move towards zero and 180 degrees. The examination of the third orientation parameter, however i.e. gamma, throws light on something different. Cell edges which were initially randomly oriented, now suddenly re-orient themselves along the directions perpendicular to its respective co-ordinate axis i.e. edges move toward 90 and 270 degrees. And this shift is quite evident, as there is no applied strain along its axis, making a drastic shift in the gamma parameter.

The examination of cell edge orientation in the off biaxial deformation leads to a slightly more significant change in alpha and beta parameters. In both, the Off-X and Off-Y deformations, one of the principal stretches is offset by a factor of two to the other. For instance, in an Off-X stretch, the RVE is deformed to twice the strain along the y axis, than it is in X. The opposite holds true for Off-Y. As a result, we observe a shift in orientation, with edges showing a slight preference in orientation, as the RVE gets stretched to its maximum deformation. In Off-Y, edges tend to align more along the x axis, as it is observed by the orange polar plot in column three. Thus, they shift to being more perpendicular to the other two axis. As we observed in the previous test, it is the gamma orientation, that is still observing a greater shift, because of the absence of any applied stretch in z. The converse holds true for the Off-X stretch as seen in the same figure.

Our study helps us make two critical observations - Firstly, in a completely isotropic microstructure, more cell edges are perpendicular to a particular co-ordinate axis than they are parallel to it. This geometric understanding helps us explain the mushroom like polar plot we see in such three dimensional structures. Secondly, our study conclusively proves that upon deformation of a microstructure such as this, cell edges tend to align themselves more towards the direction of the applied stretch. However, this re-alignment of cell edges although significant, might not showcase drastic changes in the alpha and beta polar plots, creating an illusion of rest. The same is not true for gamma plots.

## 4.2 Relative density

The second geometric parameter worth investigating would be the effect of relative density on the RVE's homogenized response. From previous literary works, we are quite aware that relative density constitutes as one of the prime factors that governs the stiffness of a material[38], [51]. The greater is the relative density of a material/cellular solid, the higher would be its resistance to deformation. In our problem, we vary the relative density in increments of one percent from one, all the way to a maximum of 4.3 percent, that is the maximum the model can attain without altering the particle density of the RVE, and at the same time not reducing the aspect ratio of the edges beyond 1/5. Keeping this in mind, we carry out the same deformations and keep a track the homogenized response of the RVE in both x and y. The response has been showcased in Fig. 4.3.

A clear trend with a direct dependence on the RVE's relative density is captured. As the relative density increases, we see a steady rise in the internal stress response of the RVE i.e. greater the relative density, more is the homogenized stress response. This increase in stiffness of the model accurately depicts what is seen in similar studies governing the effects of relative density. With increase in relative density, the microstructure clearly tends to experience larger homogenized stresses, at the same strain, indicating the fact that it is now much stiffer. This result is seen for all our three loading conditions, which further bolsters our understanding its effect.

## 4.3 Localized response

The localized response for our isotropic RVE gives a peek into the stress state within the structure. It allows us to analyze individual portions of the geometry and their stress states. This enables us with the ability to make inferences and draw correlation between the homogenized response and the intricate microstructure cell arrangement. We investigate two important indicators of stress states, namely the relation of axial stress with its local orientation and two, its relation with edge length. These two parameters constitute the prime determinants that have a strong hold on the microstructures stress state, and, as a result are investigated accordingly.

### 4.3.1 S11 vs. Orientation

To understand the influence of cell edge orientation on the axial stress it experiences can be understood by plotting a polar plot shown in Fig. 4.4. The radial angle constitutes the span of the orientation, whereas the radial distance represents the relative magnitude of the axial stress. An individual cell edge is thus represented by a scatter point lying in that range. The three individual polar plots, from left to right, show the distribution of the axial stress observed in each member as a function of the three primary orientation parameters i.e. alpha, beta and gamma, respectively (at a strain of approximately 10 percent). As a result, it helps us in analyzing whether there is a clear bias for a particular orientation, where all edges are experiencing similar stress states. The existence of such a bias can be found by looking for any asymmetric/non uniform distribution in edge stress. If such an orientation does not exist, and that there is no clear bias, what we should observe is a uniform distribution of axial stresses for any and all orientations.

For our isotropic RVE in Fig. 4.4, we make the following observations:

- Starting from the left: The distribution of S11 with alpha shows an almost uniform and symmetric distribution - almost all scatter points (represented by blue points) cover the entire domain space equally. The radial distance is also uniform, indicating that the distribution is accurate.

- The distribution is similar for the second plot. This indicates that the localized stress state is uniform across the two co-ordinate axis i.e. uniform in the plane.

- The third plot showcases greater density of more scattered cell edges at 90 degrees, than it does at the remaining orientations. This indicates that most of the elements experiences higher axial stress lie perpendicular to the z axis, or lie in planes parallel to the x-y plane. This makes a lot of sense, as the deformation the model is subjected to, is truly in x and y. There is no applied stress in z.

As we move forward with our study, it is possible that we might observe some differences when we encounter anisotropic geometries.

### 4.3.2 S11 vs. Edge length

A histogram plot of the distribution of cell edges with their frequency is plotted in the Fig. 4.5a. Next to that, a scatter plot of all edges lengths with their corresponding axial stress is provided, Fig. 4.5b. The first plot clearly showcases that a majority of the edges are in fact lying within the two micrometer range. As the edge length increases, the frequency drops almost linearly. On average in our isotropic RVE, the largest cell edge is around fourteen micrometers. With our understanding of the distribution of cell edges and their lengths, we can take a closer look at our scatter plot and try to make sense of it i.e. if there is any dependence of axial stress on edge length or not. To do so, we take weighted averages of the axial stress experienced by cell edges within a certain length, and develop a linear plot by fitting that data to a line. Doing so, enables to identify if there is any clear pattern in the change in axial stress. Now, it is always possible to have certain edges which experience an unusual magnitude of stress. However, they are not considered as anomalies and are also included in the analysis, as they represent real edges. Moreover, taking weighted averages minimizes any one time time occurrence. For our isotropic geometry for example, we observe little to no dependence on edge length. The slope of the line is slightly negative, and of the order one hundred, compared to that of the average stress experienced by all edges. The result makes sense - almost all edges are oriented randomly in the RVE, regardless of their length. They possess same cross sectional area, and similar connectivity, and as a result, experience similar stresses.

## 4.4 Anisotropy

Having analyzed isotropic geometries, it is time that we delve into the commonly observed microstructures of epithelial tissues. Our investigation of such structures helps us further our understanding in the next parameter i.e. anisotropy of cell distribution. It is our understanding that introducing a bias in the particle distribution is ultimately going to introduce the same in the cell structure. This, as a consequence, alters not only the homogenized response, but also the localized edge stresses developed within the geometry. To verify our assumption, we start by segregating the structures into in-plane and out of

plane anisotropic particle distribution. The corresponding tissue structures we end up with resemble cuboidal and stratified tissues. Once we have such geometries, we subjected them to the same in-plane stretches as seen in the previous section. We post-process the data obtained from the RVE structure and analyze the results.

### 4.4.1 Cuboidal structures: In-plane anisotropy

We start by analysing the initial orientation of the structures.

**Orientation: In-plane**

Cuboidal epithelium is seen in the inner linings of internal organs like the kidney, and gastro-intestinal linings of our digestive tissue [7]. They are single layered tissue structures, and thus showcase anisotropy only in the plane they span. To understand the full extent of anisotropy in plane, we develop four cuboidal structures of the similar dimensions and overall particle count, but ones which differ strictly in the particle distribution within the plane. To ensure that the anisotropy is limited to a single plane, our distribution of particles within the thickness is limited to one cell in a single layer. The four structures of interest include:

1. Isotropic cuboidal structure 01
    - Dimensions: 75 $\mu$m x 75 $\mu$m x 11.6 $\mu$m
    - Number of particles: 400 cells
    - Distribution density 0.27 cell per unit length in x and y, 1 cell in z
2. Anisotropic cuboidal structure 01
    - Dimensions: 75 $\mu$m x 75 $\mu$m x 11.6 $\mu$m
    - Number of particles: 395-400 cells
    - Distribution density 0.21 cell per unit length in x, 0.33 cell per unit length in y, 1 cell in z

3. Anisotropic cuboidal structure 02

   - Dimensions: 75 $\mu$m x 75 $\mu$m x 11.6 $\mu$m
   - Number of particles: 395-400 cells
   - Distribution density 0.27 cell per unit length in x, Wave pattern in y, 1 cell in z

4. Anisotropic cuboidal structure 03

   - Dimensions: 75 $\mu$m x 75 $\mu$m x 11.6 $\mu$m
   - Number of particles: 395-400 cells
   - Distribution density Wave pattern in x, Wave pattern in y, 1 cell in z

,

The particle count and outboard geometric parameters are obtained from skin histology literature [10]. All structures will thus possess on average 400 cells, with a thickness of around 11.6 micrometers. The in-plane size of the structure would be same as the RVE size we determined earlier. One thing to remember though, is that the in-plane distribution of particles is purely made up, in the interest of exploring the influence of anisotropy. Doing so, helps us develop the corresponding tissue structures that are capture all kinds of in-plane anisotropy, that can tile a two dimensional space. Once the geometry is constructed, and subjected to the requisite deformations, we start by extracting and plotting the orientation of the cell edges within the plane:

Fig. 4.6, accurately showcases the geometry and its in-plane orientation parameters (alpha and gamma). The third orientation parameter i.e. gamma is not looked at, as there is no set of edges relevant to in-plane distribution. For the first structure i.e. uniform in-plane geometry, we observe that the angle the cell makes with each of the two planar co-ordinate axis is truly uniform i.e. the alpha and beta angle distribution is spread across uniformly from zero to $2\pi$. This indicates that by developing voronoi tessellation structures around uniformly distributed particles, we develop a microstructure consisting of cell edges which are truly inform in that plane. Of course, you will have cell edges running parallel to the third

co-ordinate axis (gamma = 0) to complete the cell geometry, but they undergo compressive stresses in the third co-ordinate axis, and do not contribute directly to the homogenized response in the plane, and hence, are not shown here. This resulting distribution of alpha and beta seen in cuboidal structures is much more intuitive to the mushroom-like distribution seen in the the previous section. The is because, most of the edges we analyze here are limited to a single plane, and, with the particle density being limited to one along its thickness, introduces no extra edges being perpendicular to it.

The following three structures consists of some sort of anisotropic particle distribution in the plane. The second structure has anisotropy introduced by changing the particle density along each co-ordinate axis. It consists, on average sixteen particles along the x axis, and around twenty-five particles along the y axis, with the overall particle density remaining constant at four hundred cells per RVE. The result of such a particle distribution is an anisotropic microstructure. It is observed that increasing the particle density along the y axis has introduced several cell edges lying perpendicular to it. This conclusion is drawn by looking at the alpha orientation, being lob-sided towards zero and $\pi$. Similarly, with a lesser density along x axis, results in lesser particles along y and more perpendicular to it. This is evident by the beta orientation.

The third structure consists of a wave like-particle distribution along the y axis, and a random uniform particle distribution along the other (x axis). The wave pattern in the y axis is brought about by distributing a select bunch of particles normally about a sequence of points. The resulting structure also has the same particle density, but a very clear bias in its orientation, as can be seen from the figure. Most cell edges end up lying perpendicular to the x axis, and parallel to the y axis. This is going to lead to some very interesting homogenized behavior. The fourth structure of interest is one that possess a wave like distribution along both the x and the y axis. The resulting orientation is somewhat uniform, but having a slight bias towards the x axis.

Having examined the in-plane edge orientations, we can move on to analyze their effects on the homogenized response.

**Homogenized response**

We start with the isotropic structure. Performing a equi-biaxial stretch to the structure, shows us that the homogenized stress response in both the x and y direction is exactly the same as seen in Fig. 4.7. As we move toward the off biaxial stretches, we start to observe a minute deviation in the homogenized response between x and y. The model seems to be showcasing marginally higher stresses in the y direction, as compared to the stress in the x direction in the off biaxial stretch in x. The opposite is seen, when the same microstructure is subjected to an off biaxial stretch with a bias in y. The discrepancy, although minute, is present in the first structure.

The second structure, as we had concluded in our previous study showcases a clear bias as it is stretched in the plane. For instance, upon subjecting the model to equi-biaxial stretches, the homogenized stress observed along the x axis is much higher as compared to the y axis. This result is in terms with the in-plane orientation that we discussed earlier. With the majority of elements lying along he x axis, reaction force of those edges will be significantly higher. Thus, as a consequence, these members will experience a greater stress state. The explanation holds true, as we sweep through the remaining two deformation states. In both the off biaxial stretches, it is the homogenized response along the x axis, which is significantly larger, as compared to the response along y axis. The third structure, showcasing the highest degree of anisotropy, has a similar outcome on its homogenized response. The wave like pattern along the y axis has essentially resulted in a multitude of cell edges lying parallel along the y axis, as compared to the x axis. As a result, when the structure is subjected to an equi biaxial stretch, the homogenized response along the y axis is clearly larger to its response along x. The same pattern repeats for the remaining two loading conditions. Our fourth and final structure, showcases a uniform response within the plane when subjected to equi-biaxial stretch, but its response differs drastically when compared to the first model. This is essentially true for the remaining two deformation studies i.e. off biaxial stretches in x and y. There is a clear difference in the homogenized response in x and y.

### S11 vs. Edge length

As investigated previously for the isotropic RVE, we study the relation between edge length and the axial stresses experienced by the cell edges, for cuboidal tissue structures. The frequency distribution of the edges is necessary to ensure that we take the weighted bias of every cell edge's axial stress response, while determining S11 dependence. Doing so, leads us to the following relation, as seen in Fig. 4.8. The frequency of cell edges with lengths less than 4-6 $\mu$m is extremely high. It is our understanding that those particular cell edges lie on the surface plane of the cuboidal structures. This is true, because of the distribution pattern followed for constructing these geometries - The cell density in z is limited to one, which means that the resultant voronoi subspace is not going to contain cell edges inside the geometry, which are parallel to the x-y plane. All of them will lie on the top and bottom planes. The only edges running through the geometry are going to be those perpendicular to the surface. And since they face no opposition, they are usually long and slender beams. Our analogy holds true for the first two structures, as we see a peak in frequency for cell edges longer than 10 $\mu$m (which is close to the thickness of the structure). This information becomes helpful as we study the third column i.e. S11 response to edge lengths.

In all of our four planar microstructures, we observe that there is an inverse relation between the axial stress experienced by the cell edges and the edge lengths. The red line provides the trend. This means, that the smaller edges in general experience much greater stresses, when compared to longer ones. Referring back to the second column in Fig. 4.8, helps us make a second inference. Smaller edges i.e. edges lying on the surface seem to endure much greater stresses than their longer counterparts. This means that that stress concentrations within similar microstructures lie at the surface, when they are subjected to in-plane strains.

### S11 vs. Orientation

Fig. 4.9. showcases the axial stresses experienced by all cell edges, and the orientation they lie at, at a fixed strain of 10 percent. This particular plot showcases the stress distribution for off biaxial stretch, with a bias in x. From left to right, the first plot shows a high

density of cell edges lying close at zero or $\pi$ to the x axis. Their axial stresses are significantly higher, as opposed to cell edges lying perpendicular to it. With our understanding of change in orientation, we that increasing the deformation further, will result in edges aligning more and more along the x axis. This includes even the edges lying perpendicular to it. Moving to the next plot, we see the distribution of cell edges with beta. A significant portion of edges seem to be lying at $\pi/2$. Their magnitudes of axial stress is also high as compared to those lying along 0 and $\pi$. This is true, because the extent of stretch in y is much smaller than it is in x.

Now, we made an assumption about the distribution of edge lengths with their orientation in the previous section. Our justification of the same, can be inferred from the third polar plot from Fig. 4.9. It looks like most of the elements experiencing any significant amount of axial stress lies perpendicular to the z axis. Those that lie along the axis, experience very little stress in comparison. Thus, we can safely conclude that the scatter plots from Fig. 4.8 in the first half, represent planar edges.

### 4.4.2 Stratified structures: Out of plane anisotropy

Our next section focuses on epithelial tissues which possess out of plane anisotropy. Two common microstructures that come to mind are the stratified and pseudo-stratified microstructures. These structures are known to exhibit some kind of bias in the particle distribution along their thickness i.e. along the z axis [10], [52], [53]. To replicate the same, we develop their corresponding micro-structures and subject them to the same deformations as seen before and track their homogenized and localized response. The characteristics of the two geometries is listen below:

1. Stratified structure
    - Dimensions: 75 $\mu$m x 75 $\mu$m x 75 $\mu$m
    - Particle density: 800 cells
    - Distribution: Random in x and y, exponential distribution in z
2. Pseudo stratified structure

- Dimensions: 75 $\mu$m x 75 $\mu$m x 11.6 $\mu$m
- Particle density: 400 cells
- Distribution: Random in x and y, normal distribution in z with two peaks

**Homogenized response**

Fig. 4.10 gives an insight into the in plane response of these structures. The equi biaxial plot of the stratified epithelial structure shows us that the response in both x and y are very similar. This is somewhat true for the second structure. The behavior, although very similar, seems to have some inherent anisotropy present within it. Now, it is our understanding that the result of this might be purely coincidental, and might not have a significant relation to the distribution in z. As we move forward to the next two set of deformations, the stratified structure behaves, as any in plane isotropic geometry would i.e. possessing almost similar responses in both x and y, as the structure is subjected to different stresses. The same should be technically true for the second geometry as well, i.e. the pseudo stratified structure.

We can thus conclude, that any significant anisotropic behavior of a microstructure is purely a result of the particle distribution in the plane, and not out of plane.

**S11 vs. Edge length**

While the homogenized response in the z direction is not particularly helpful, breaking it apart and analyzing the distribution of stresses with it, might have some merit. For instance, an important question one can ask would to be to study if keratinized skin tissues observe any gradient in the localized stresses along the thickness, when such a structure is subjected to in plane stretches. One way to investigate that would be by taking a look at Fig. 4.11, to get some insight into the effect of anisotropy.

We know that that the stratified structure observes an exponential distribution of cell particles through the thickness i.e. the density is maximum at the top face, while it is exponentially lower at the bottom face. This disparity of distribution is translated to edge lengths as well, as seen in Fig. 4.11 (Row 1, Column 1). Edges ranging from 0 to 5 $\mu$ m are in largest numbers, whereas consequent edges have exponentially lower frequencies. With

both this knowledge, we can conclusively say that larger edges lie closer to the bottom face, and smaller edges (more in number), lie closer to the top. The information proves helpful as we investigate the second plot for stratified geometries (Row 1, Column 2). The S11 vs. edge length plot trend, represented by the solid red line„ shows a negative trend. Smaller edges i.e. the top surface experiences greater stresses, as compared edges lying closer to the bottom. Thus, a clear gradient in particle distribution has ultimately resulted in a gradient in localized stresses as well.

The pattern of stress distributions is very similar even for the pseudo-stratified geometry, indicating the fact that smaller edges endure larger stresses. So, if there is an induced anisotropy in particle distribution, there will be a gradient in localized stresses as well.

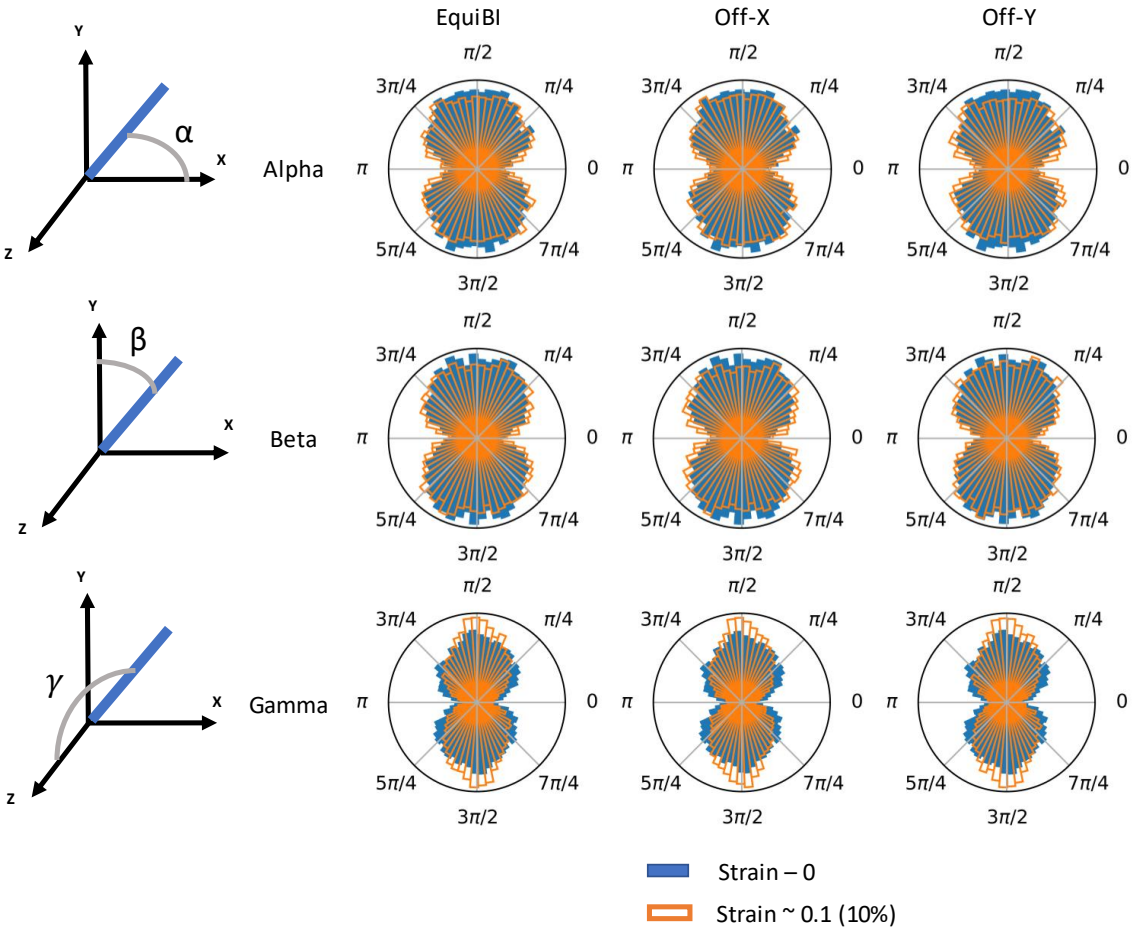


**Figure 4.2.** Distribution of cell edge orientations for all three deformations (columns): The deep plot in blue bar plot showcases initial orientation i.e. at strain = 0. The overlapped orange plot provides the revised orientation at strain = 0.1 (10 percent). First row: Alpha, Second row: Beta, and Third row: Gamma

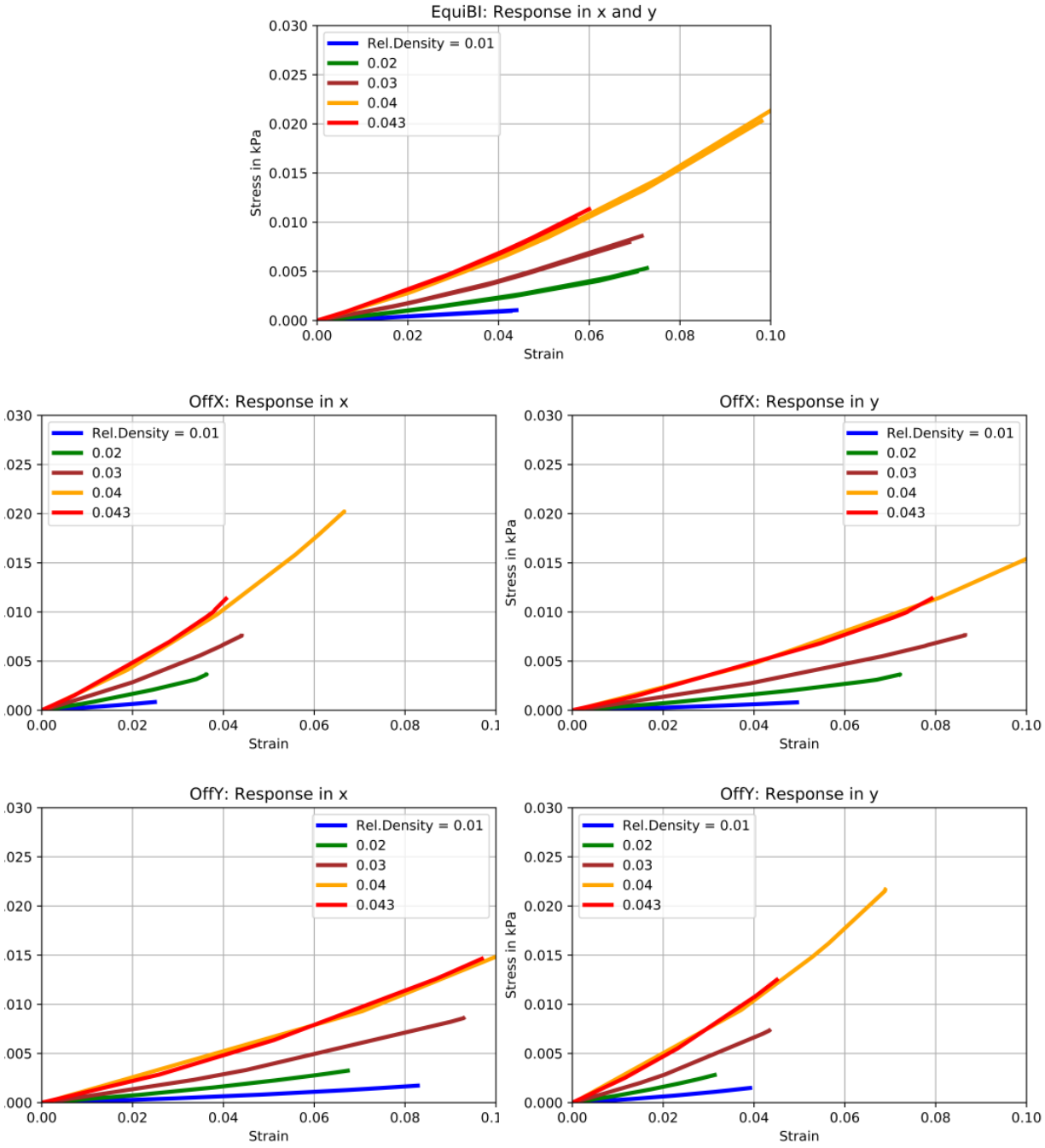


**Figure 4.3.** Variation of relative density from 1 percent to a geometry allowed maximum of 4.3 percent. Plots provided for all three deformations.

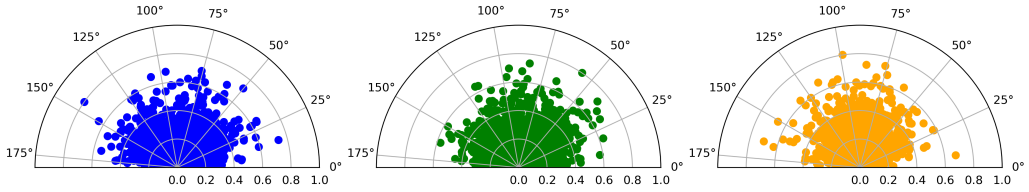


**Figure 4.4.** Localized response: S11 vs. Orientation (Alpha, beta and gamma)

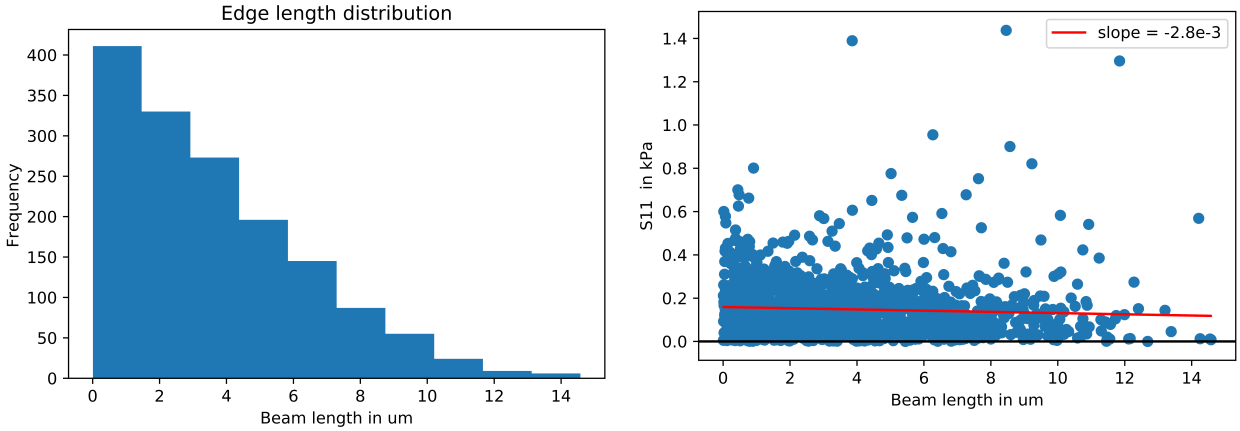


(a) Frequency distribution of edge lengths

(b) Scatter plot of cell edge axial stress with edge length

**Figure 4.5.** Localized response: S11 vs. Edge length

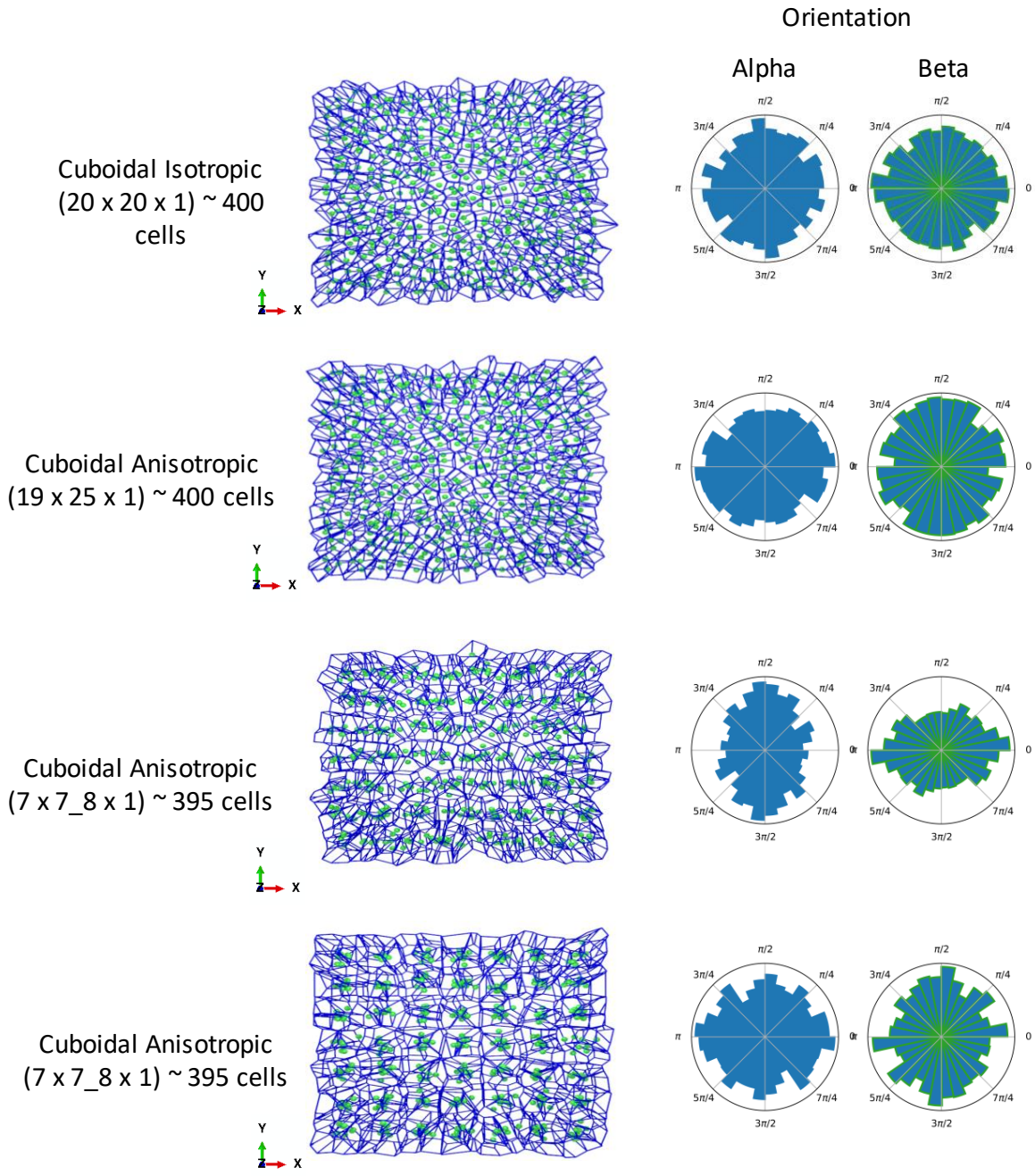


**Figure 4.6.** Microstructure and orientation of all four anisotropy geometries, and their corresponding in-plane initial orientations (alpha and beta polar plots)

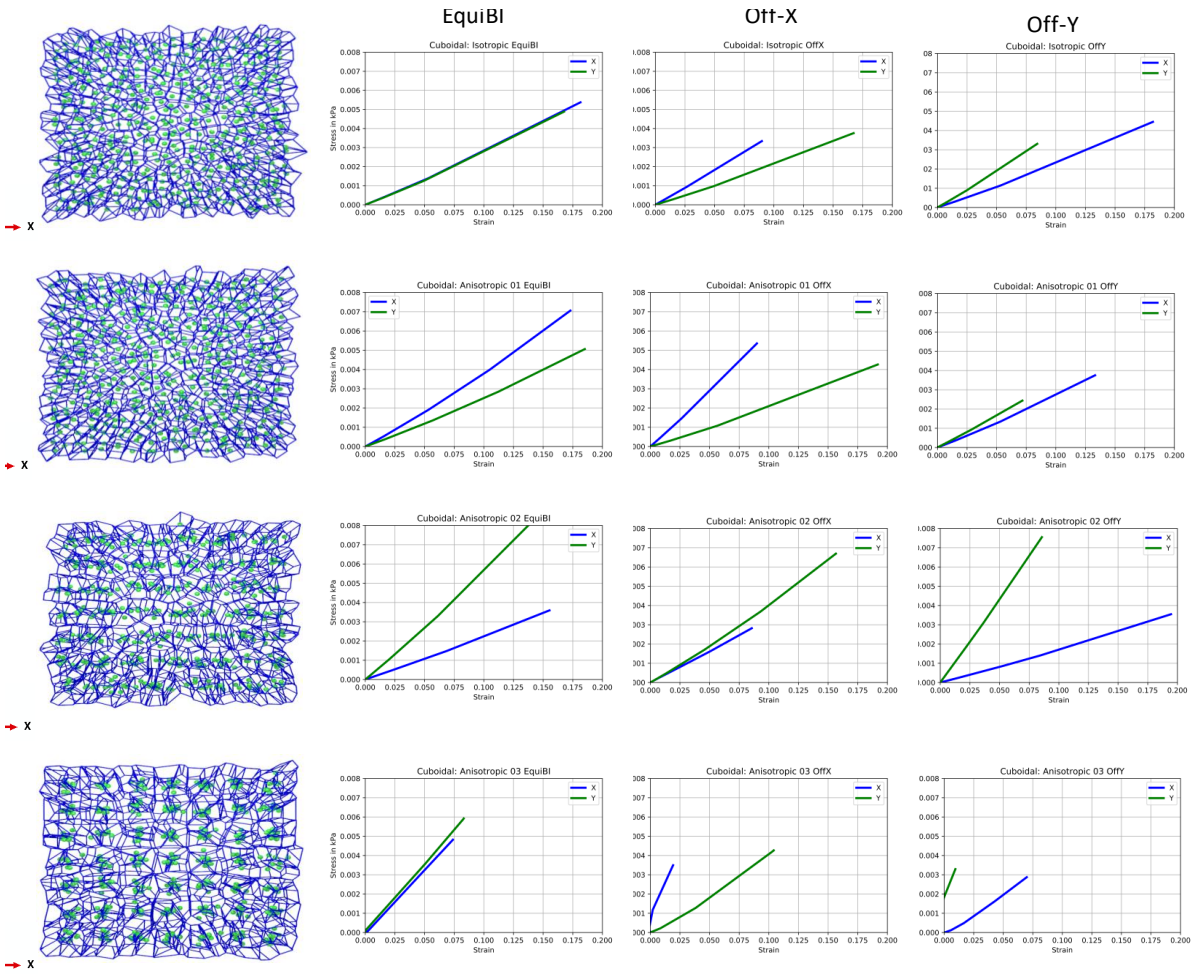


**Figure 4.7.** In plane homogenized response of the four cuboidal structures. The flow of data follows previous figures: First row - Isotropic, subsequent rows - In-plane anisotropic structures.

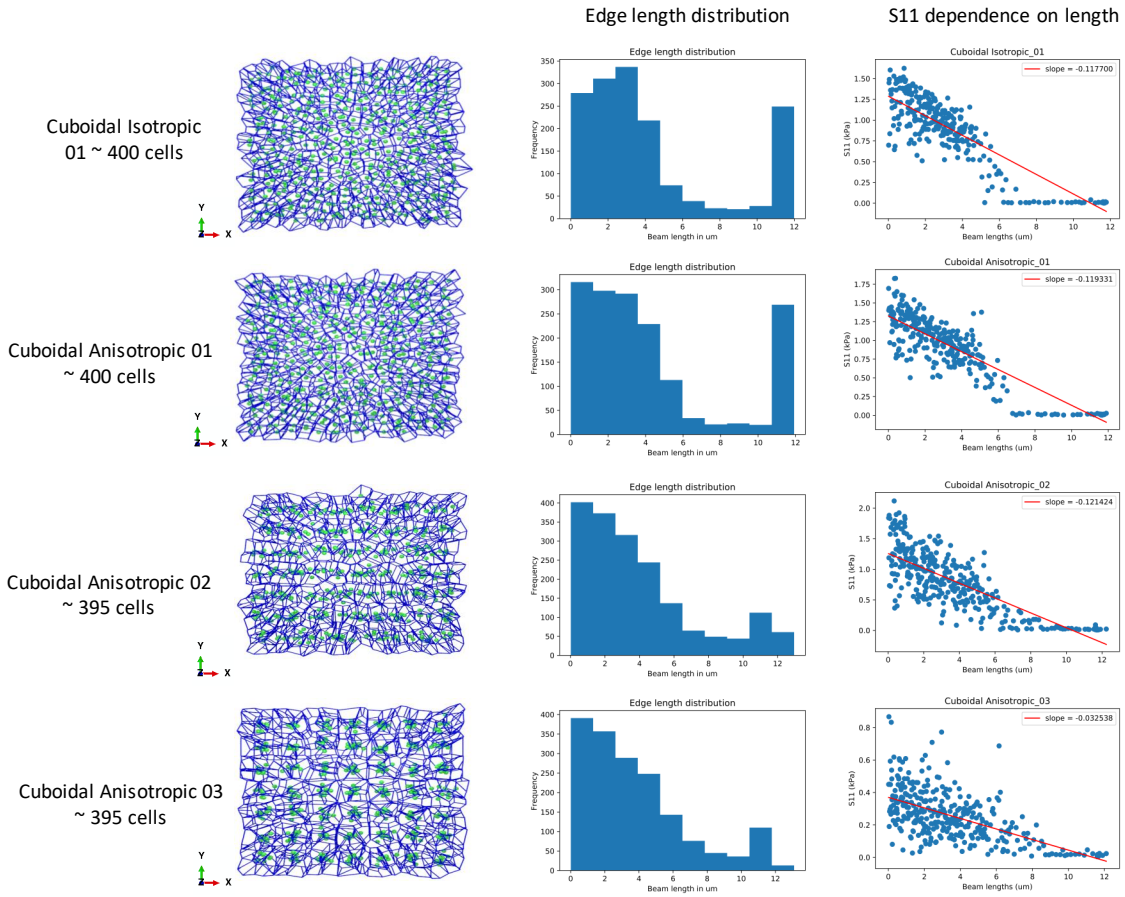


**Figure 4.8.** Cuboidal structures: Frequency distribution of edge length and dependence of axial stress with edge length.

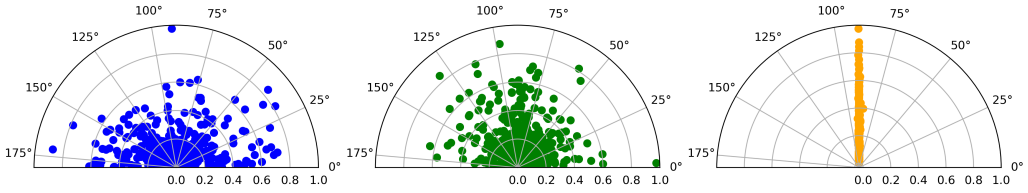


**Figure 4.9.** Axial stress distribution of cell edges across three orientation parameters - alpha, beta and gamma

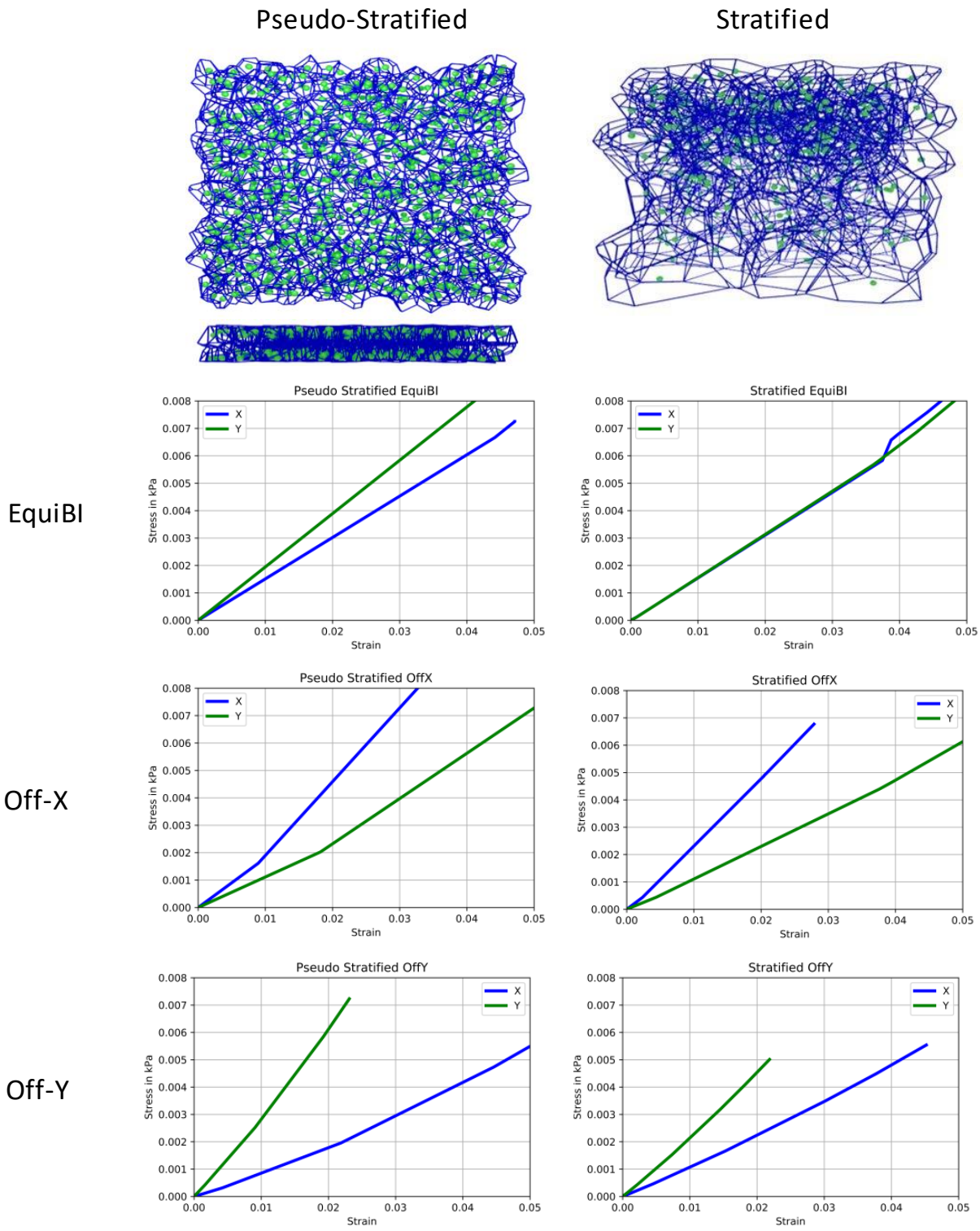


**Figure 4.10.** Stratified epithelial tissue structures: Homogenized response

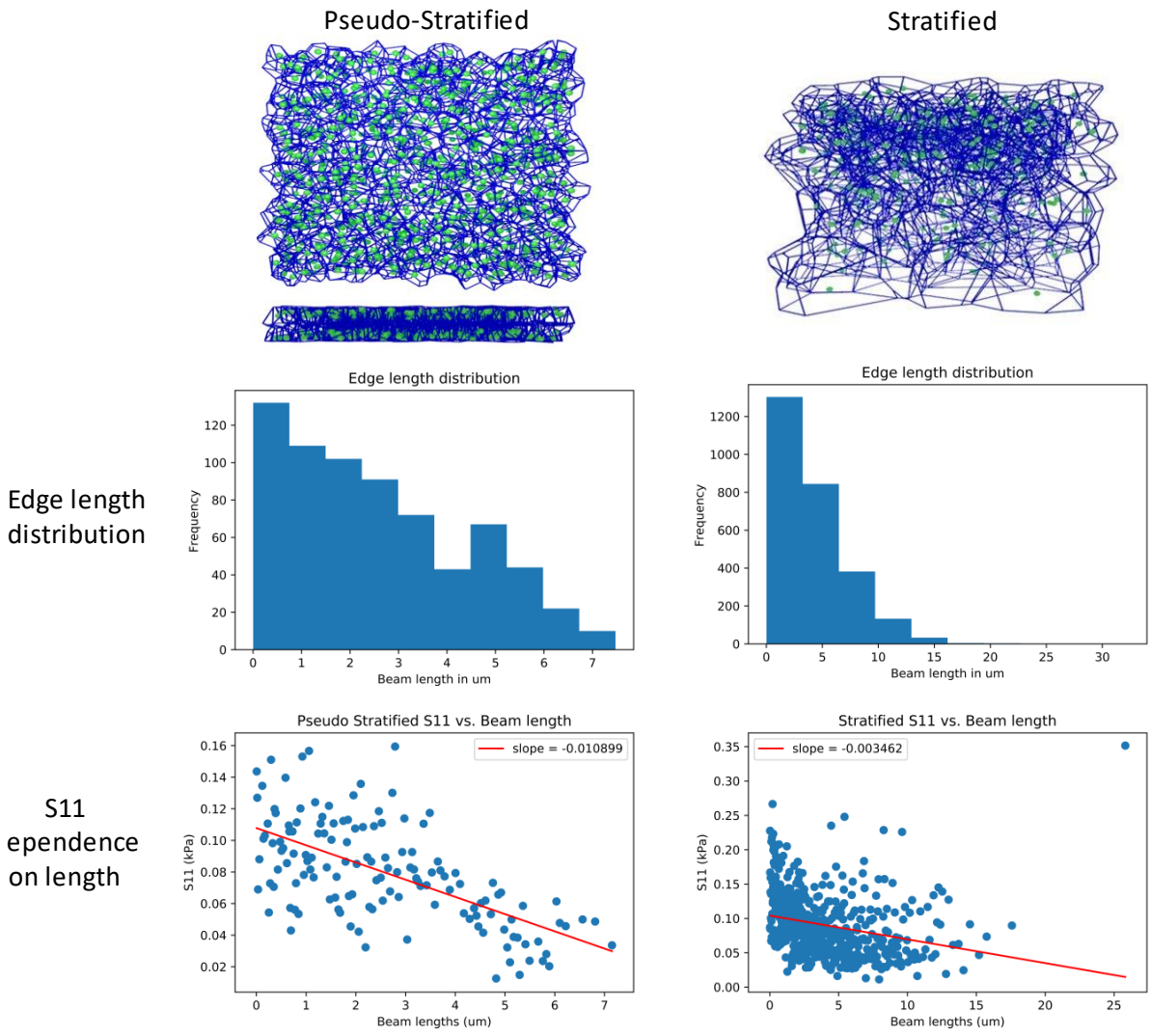


**Figure 4.11.** Stratified epithelial tissue structures: Edge length frequency distribution and S11 dependence on length.

# 5. CONCLUSION AND FUTURE WORK

The objective of this thesis was to develop a deeper understanding of the geometric parameters of bio-inspired tissue structures and document their influence on the structure's micro-mechanical response. The first challenge in carrying out this study, was developing a geometrically accurate microstructure that incorporated most of the features of the tissue. The process of doing so resulted in making a lot of assumptions, like characterizing and shortlisting important geometric features that best captured the elastic deformation of these tissues, while sidelining certain biological and physiological features that would hinder the decision making process, or make the model unnecessarily complex. The parameters that were shortlisted included the cell orientation, cell edge length, cell distribution (isotropy/anisotropy), connectivity and relative density. Meanwhile, biological factors like cell division, dynamic cell re-arrangement, intercellular cadherin cell-adhesion and intracellular cell compression pressure were not included. The process of doing so, would help separate the biological factors from the intended geometric study, making the analysis cleaner, but, at the same time, implicate the study to bio-inspired micromechanics, rather than micromechanics in general. Thus, the geometry we develop and analyze in our work is a three dimensional open foam microstructure, with cell edges represented as 3D beam elements, and cell vertices represented by joints with finite elastic stiffness.

In Chapter 2, we focus on scripting open foam microstructures from the Voro++ interface to ABAQUS. The process flow of creating the geometry begins with specifying the particle distribution and the volume space for the microstructure. Doing so enables the system to develop multiple three dimensional voronoi subspaces, that virtually hug a particle to their closest proximity. Their boundaries of intersecting spaces are thus represented by a combination of vertices and their cell edges - this separates cell spaces from one another. The resulting geometry is a voronoi tessellation. This representation of cell edges, in the form of poly lines, is then scripted into the ABAQUS environment via Python, to finally result in our open foam microstructure. Our resulting geometry is capable of capturing all the necessary geometric variables, which we are interested in learning. Cell distribution is a user defined value prescribed prior to generating the model. Cell edges are represented

by beams/wires in the microstructure. Their corresponding length serves as our second parameter. The connectivity can be calculated by determining the number of cell edges that intersect at each node. The orientation can be prescribed by taking a dot product of the cell edge vector with our preferred co-ordinate axes, giving us our three crucial orientation parameters i.e. alpha, beta and gamma. And finally, relative density can be determined by taking the ratio of the space occupied by the voronoi tessellation to the overall volume space of our microstructure.

In this manner, all our crucial parameters are now defined, and we can comfortably describe the deformation behavior of tissues now. Out of the biological parameters we excluded in our study, it is the intercellular pressure that can also be considered as a geometric parameter that affects deformation. Our model does not capture that. This is indeed a limitation. The only methodology of including it would be by developing a closed foam voronoi tessellation. And the volume within each space could be monitored and controlled via penalty methods, mimicking a more realistic cell. This process was pursued for a while. The transition of open to close foam structure would entail that the geometry would now be represented by 3D shells instead of beams and rigid vertices. The shells would be interconnected, thereby creating pockets of isolated volume, where the pressure inside the cell could be mimicked by penalty methods. This analogy, although promising has its fair share of drawbacks - for instance, replacing beam edges completely would mean that our ability to capture other equally crucial parameters like cell orientation, connectivity and relative density would diminish. Capturing accurate deformations is not the only agenda - it is quantifying and characterizing it that is also important. The process of doing so with just shells is hard. One would thus need to develop a combination of the two models and capture that uniquely, without altering the actual deformation of the microstructure. As a result, the concept of closed foam microstructure was dropped. However, this still remains as one of our future works.

Our geometry creation concludes after we make our final inclusion i.e. adding periodic boundary surfaces, and we move on to developing a finite element model for our study. More so, a Representative Volume Element (RVE) as we deal with deformation of structures that span an entire sub-space. In the process of developing an RVE, we come across one factor

that might hinder our study i.e. boundary effects. With our inability to apply periodic boundary conditions to the faces, we face the threat of boundary effects from creeping in. While periodic boundary surfaces do help in alleviating some boundary effects, we decide to minimize it by staggering our RVE geometry, by developing an RVE within an RVE. As a result, we take on the task of iterating and modifying both RVE dimensions, until statistical homogeneity is met and boundary effects are minimized in the system. Chapter 3 delves deep into the analysis of the same. The exact process falls down to building three different outer box geometries and selecting three different Inner RVE dimensions. A combination of 9 configurations are analyzed and the one satisfying both conditions is chosen as a the appropriate RVE. To eliminate variation in data, a total of 5 samples of each configuration are generated. The entirety of the third chapter provides an in-depth comparison of the nine configurations, and concludes with Configuration 2 as the prime RVE structure.

Chapter 4 delves into the geometric study of all microstructures. We learn that the initial orientation of a microstructure is dependent on the distribution of cells in a medium. As a result, uniform random distribution of cells should ultimately yield a similar uniform distribution of cell edges within, resulting in similar alpha, beta and gamma distribution of angles. And we observe the same as we develop a uniformly random distributed structure. Understanding beam orientations in three dimensions gives us an insight on how to interpret the plot themselves. This becomes useful as we plot the distribution of alpha, bet and gamma and observe that although they appear non uniform (mushroom profile), they are in fact random and equally distributed. The bias is seen purely because of the dimension of the space. Increasing the dimension from three, will further skew the bias, which decreasing it removes it. As a result, we see this profile emerge only for three or higher dimension geometries. However it is not seen in planar two dimensional geometries. It is upon the application of some deformation, that we learn more about cell re-orientation and change. Upon studying three different types of deformations, we can safely conclude that a cell edge orients itself along the direction of stretch. And the extent of this re-orientation is going to be widely dependent on the strain it is subjected to. The study also confirms our understanding on the effect of relative density on the homogenized response of the structures. Increasing relative density, increases the stiffness and stress response of the microstructure. The stiffness

will eventually rise towards the material stiffness as the relative density moves towards 1. The localized response provides no significant insight for isotropic geometries. We do not observe any clear dependence of axial stresses on orientation or edge length, and move on to our final study on anisotropy.

Anisotropy constitutes the final section in our chapter, as it investigates the degree of influence of all the geometric parameters. Two common epithelial structure types are modelled and scrutinized - cuboidal planar epithelial tissue structures, and stratified epithelial tissue structures. Cuboidal structures observe in plane cell distribution, and as a result, observe only planar anisotropy. Stratified structures, on the other hand, observe out of plane anisotropy, or variation along its thickness. The separation of the two, helps identify the degree of influence for each individually. While real life tissue like the keratinized epithelial tissue structure observes both in plane and out of plane, anisotropy, this combination is not analyzed here. But our study should be able to concur the same. We observe that introducing anisotropy in the plane has a significant impact on both - cell edge orientation, and its homogenized response in the plane. We see that structures with cell edges oriented more towards a principal axis observe a higher stiffness and stresses. The converse is true, for cell edges oriented more towards the perpendicular direction i.e. they observe significantly lesser stresses for the same amount of strain. This helps draw a correlation between cell edge orientation and its corresponding homogenized response, which in turn relates cell particle distribution with its homogenized response. Investigating dependence of axial stresses within the geometry on its cell edge length and orientation also provides some good insight into the localized stress distribution within the structure. The axial stress endured by a cell edge has an inverse dependence on its length. Thus, smaller edges experience greater stresses, while longer edges experience lower stresses. A peak into the distribution of cell orientation, further helps us identify the region of peak stress. It is seen that the surfaces of such structures observe greater in plane stresses than the inner edges, which proves that stresses are usually concentrated on the surface.

Observing localized response in out-of-plane anisotropic geometries teaches us about the gradient of stress that exists along its thickness. Stratified geometries, like cuboidal structures, also observe an inverse relation of axial stress on edge length. As a result, it is

the top surface of the structure that truly experiences higher stresses. But, unlike cuboidal structures, stratified geometries have a gradient of particle distribution along the thickness, which in turn translates to gradient in edge lengths. This concludes that, a gradient in the localized stress along z exists.

In all, our proposed method satisfies our two primary objectives conclusively. It captures almost all geometric parameters effectively, and also provides a detailed insight on the micro structure's homogenized and localized response. However, it falls short on design validation. As the model is an imitation of the epithelial tissue structure without the osmotic pressure a blatant comparison of our method with existing microstructure models would be un-warranted. Thus, to truly get a grasp of its effective methodology, the model has to be either adapted to account for the osmotic pressure (by introducing a penalty function on volume, or by integrating shells to close cell volumes, as discussed previously) or by testing its design with existing open foam methodologies in the literature. Going down the experimental route of either 3D printing the microstructures or generating them using innovative foaming technologies would also would also be interesting to implement and study.

# REFERENCES


[1] *H&E stain of biopsy of normal esophagus showing the stratified squamous cell epithelium.* Aug. 2006.

[2] H. F. Gómez, M. S. Dumond, L. Hodel, R. Vetter, and D. Iber, "3D cell neighbour dynamics in growing pseudostratified epithelia," *eLife*, vol. 10, 2021, ISSN: 2050084X. DOI: 10.7554/elife.68135.

[3] P. Gómez-Gálvez, P. Vicente-Munuera, A. Tagua, C. Forja, A. M. Castro, M. Letrán, A. Valencia-Expósito, C. Grima, M. Bermúdez-Gallardo, Ó. Serrano-Pérez-Higueras, F. Cavodeassi, S. Sotillos, M. D. Martín-Bermudo, A. Márquez, J. Buceta, and L. M. Escudero, "Scutoids are a geometrical solution to three-dimensional packing of epithelia," *Nature Communications*, vol. 9, no. 1, 2018, ISSN: 20411723. DOI: 10.1038/s41467-018-05376-1.

[4] P. Gómez-Gálvez, P. Vicente-Munuera, S. Anbari, J. Buceta, and L. M. Escudero, *The complex three-dimensional organization of epithelial tissues*, 2021. DOI: 10.1242/dev.195669.

[5] C. Hagios, A. Lochter, and M. J. Bissell, "Tissue architecture: The ultimate regulator of epithelial function?" *Philosophical Transactions of the Royal Society B: Biological Sciences*, vol. 353, no. 1370, 1998, ISSN: 09628436. DOI: 10.1098/rstb.1998.0250.

[6] W. T. Gibson and M. C. Gibson, *Chapter 4 Cell Topology, Geometry, and Morphogenesis in Proliferating Epithelia*, 2009. DOI: 10.1016/S0070-2153(09)89004-2.

[7] T. Mochizuki, S. Suzuki, and I. Masa, "Spatial pattern of cell geometry and cell-division orientation in zebrafish lens epithelium," *Biology Open*, vol. 3, no. 10, 2014, ISSN: 20466390. DOI: 10.1242/bio.20149563.

[8] S. Hilgenfeldt, S. Erisken, and R. W. Carthew, "Physical modeling of cell geometric order in an epithelial tissue," *Proceedings of the National Academy of Sciences of the United States of America*, vol. 105, no. 3, 2008, ISSN: 00278424. DOI: 10.1073/pnas.0711077105.

[9] M. J. Honda, Y. Sumita, H. Kagami, and M. Ueda, "Histological and immunohistochemical studies of tissue engineered odontogenesis," *Archives of Histology and Cytology*, vol. 68, no. 2, 2005, ISSN: 09149465. DOI: 10.1679/aohc.68.89.

[10] A. Vela-Romera, V. Carriel, M. A. Martín-Piedra, J. Aneiros-Fernández, F. Campos, J. Chato-Astrain, N. Prados-Olleta, A. Campos, M. Alaminos, and I. Garzón, "Characterization of the human ridged and non-ridged skin: a comprehensive histological, histochemical and immunohistochemical analysis," *Histochemistry and Cell Biology*, vol. 151, no. 1, 2019, ISSN: 1432119X. DOI: 10.1007/s00418-018-1701-x.

[11] M. Sand, T. Gambichler, D. Sand, M. Skrygan, P. Altmeyer, and F. G. Bechara, *MicroRNAs and the skin: Tiny players in the body's largest organ*, 2009. DOI: 10.1016/j.jdermsci.2008.10.004.

[12] C. Stowers, T. Lee, I. Bilionis, A. K. Gosain, and A. B. Tepole, "Improving reconstructive surgery design using Gaussian process surrogates to capture material behavior uncertainty," *Journal of the Mechanical Behavior of Biomedical Materials*, vol. 118, 2021, ISSN: 18780180. DOI: 10.1016/j.jmbbm.2021.104340.

[13] A. M. Zöllner, A. B. Tepole, A. K. Gosain, and E. Kuhl, "Growing skin: Tissue expansion in pediatric forehead reconstruction," *Biomechanics and Modeling in Mechanobiology*, vol. 11, no. 6, 2012, ISSN: 16177959. DOI: 10.1007/s10237-011-0357-4.

[14] G. Albu, B. Babik, K. Késmárky, M. Balázs, Z. Hantos, and F. Peták, "Changes in Airway and Respiratory Tissue Mechanics After Cardiac Surgery," *Annals of Thoracic Surgery*, vol. 89, no. 4, 2010, ISSN: 00034975. DOI: 10.1016/j.athoracsur.2009.12.062.

[15] M. Geerligs, *Skin layer mechanics*, 2010. 2010.

[16] B. Hansen and G. B. Jemec, "The mechanical properties of skin in osteogenesis imperfecta," *Archives of Dermatology*, vol. 138, no. 7, 2002, ISSN: 0003987X. DOI: 10.1001/archderm.138.7.909.

[17] S. Iravanimanesh, M. A. Nazari, F. Jafarbeglou, M. Mahjoob, and M. Azadi, "Extracting the elasticity of the human skin in microscale and in-vivo from atomic force microscopy experiments using viscoelastic models," *Computer Methods in Biomechanics and Biomedical Engineering*, vol. 24, no. 2, 2021, ISSN: 14768259. DOI: 10.1080/10255842.2020.1821000.

[18] G. D. O'Connell, S. Sen, and D. M. Elliott, "Human annulus fibrosus material properties from biaxial testing and constitutive modeling are altered with degeneration," *Biomechanics and Modeling in Mechanobiology*, vol. 11, no. 3-4, 2012, ISSN: 16177959. DOI: 10.1007/s10237-011-0328-9.

[19] S. Okuda, Y. Inoue, M. Eiraku, Y. Sasai, and T. Adachi, "Reversible network reconnection model for simulating large deformation in dynamic tissue morphogenesis," *Biomechanics and Modeling in Mechanobiology*, vol. 12, no. 4, 2013, ISSN: 16177959. DOI: 10.1007/s10237-012-0430-7.

[20] L. McNamara, "Biologically inspired and biomolecular materials," *Comprehensive biomaterials*, 2011.

[21] W. Xi, T. B. Saw, D. Delacour, C. T. Lim, and B. Ladoux, *Material approaches to active tissue mechanics*, 2019. DOI: 10.1038/s41578-018-0066-z.

[22] A. G. Fletcher, M. Osterfield, R. E. Baker, and S. Y. Shvartsman, *Vertex models of epithelial morphogenesis*, 2014. DOI: 10.1016/j.bpj.2013.11.4498.

[23] S. Alt, P. Ganguly, and G. Salbreux, *Vertex models: From cell mechanics to tissue morphogenesis*, 2017. DOI: 10.1098/rstb.2015.0520.

[24] T. Lecuit and P. F. Lenne, *Cell surface mechanics and the control of cell shape, tissue patterns and morphogenesis*, 2007. DOI: 10.1038/nrm2222.

[25] G. K. Xu, Y. Liu, and B. Li, "How do changes at the cell level affect the mechanical properties of epithelial monolayers?" *Soft Matter*, vol. 11, no. 45, 2015, ISSN: 17446848. DOI: 10.1039/c5sm01966d.

[26] N. Murisic, V. Hakim, I. G. Kevrekidis, S. Y. Shvartsman, and B. Audoly, "From Discrete to Continuum Models of Three-Dimensional Deformations in Epithelial Sheets," *Biophysical Journal*, vol. 109, no. 1, 2015, ISSN: 15420086. DOI: 10.1016/j.bpj.2015.05.019.

[27] G. Charras and A. S. Yap, *Tensile Forces and Mechanotransduction at Cell–Cell Junctions*, 2018. DOI: 10.1016/j.cub.2018.02.003.

[28] K. C. Hart, J. Tan, K. A. Siemers, J. Y. Sim, B. L. Pruitt, W. J. Nelson, and M. Gloerich, "E-cadherin and LGN align epithelial cell divisions with tissue tension independently of cell shape," *Proceedings of the National Academy of Sciences of the United States of America*, vol. 114, no. 29, 2017, ISSN: 10916490. DOI: 10.1073/pnas.1701703114.

[29] A. Nestor-Bergmann, G. A. Stooke-Vaughan, G. K. Goddard, T. Starborg, O. E. Jensen, and S. Woolner, "Decoupling the Roles of Cell Shape and Mechanical Stress in Orienting and Cueing Epithelial Mitosis," *Cell Reports*, vol. 26, no. 8, 2019, ISSN: 22111247. DOI: 10.1016/j.celrep.2019.01.102.

[30] E. V. van Leen, F. di Pietro, and Y. Bellaïche, *Oriented cell divisions in epithelia: from force generation to force anisotropy by tension, shape and vertices*, 2020. DOI: 10.1016/j.ceb.2019.07.013.

[31] J. B. Jonas, K. Ohno-Matsui, L. Holbach, and S. Panda-Jonas, "Retinal pigment epithelium cell density in relationship to axial length in human eyes," *Acta Ophthalmologica*, vol. 95, no. 1, 2017, ISSN: 17553768. DOI: 10.1111/aos.13188.

[32] M. Huzaira, F. Rius, M. Rajadhyaksha, R. R. Anderson, and S. González, "Topographic variations in normal skin, as viewed by in vivo reflectance confocal microscopy," *Journal of Investigative Dermatology*, vol. 116, no. 6, 2001, ISSN: 0022202X. DOI: 10.1046/j.0022-202X.2001.01337.x.

[33] C. H. Rycroft, *VORO++: A three-dimensional Voronoi cell library in C++*, 2009. DOI: 10.1063/1.3215722.

[34] T. D. Fenn, D. Ringe, and G. A. Petsko, "POVScript+: A program for model and data visualization using persistence of vision ray-tracing," *Journal of Applied Crystallography*, vol. 36, no. 3 II, 2003, ISSN: 00218898. DOI: 10.1107/S0021889803006721.

[35] F. Concha, M. Sarabia-Vallejos, and D. E. Hurtado, "Micromechanical model of lung parenchyma hyperelasticity," *Journal of the Mechanics and Physics of Solids*, vol. 112, 2018, ISSN: 00225096. DOI: 10.1016/j.jmps.2017.11.021.

[36] F. S. Cavalcante, S. Ito, K. Brewer, H. Sakai, A. M. Alencar, M. P. Almeida, J. S. Andrade, A. Majumdar, E. P. Ingenito, and B. Suki, "Mechanical interactions between collagen and proteoglycans: Implications for the stability of lung tissue," *Journal of Applied Physiology*, vol. 98, no. 2, 2005, ISSN: 87507587. DOI: 10.1152/japplphysiol.00619.2004.

[37] R. J. Boulbes, *Troubleshooting Finite-Element Modeling with Abaqus*. 2020. DOI: 10.1007/978-3-030-26740-7.

[38] L. J. Gibson, "Cellular solids," *MRS Bulletin*, vol. 28, no. 4, 2003, ISSN: 08837694. DOI: 10.1557/mrs2003.79.

[39] W. Y. Jang, A. M. Kraynik, and S. Kyriakides, "On the microstructure of open-cell foams and its effect on elastic properties," *International Journal of Solids and Structures*, vol. 45, no. 7-8, 2008, ISSN: 00207683. DOI: 10.1016/j.ijsolstr.2007.10.008.

[40] C. San Marchi and A. Mortensen, "Deformation of open-cell aluminum foam," *Acta Materialia*, vol. 49, no. 19, 2001, ISSN: 13596454. DOI: 10.1016/S1359-6454(01)00294-4.

[41] A. Bacigalupo and L. Gambarotta, "Homogenization of periodic hexa- and tetrachiral cellular solids," *Composite Structures*, vol. 116, no. 1, 2014, ISSN: 02638223. DOI: 10.1016/j.compstruct.2014.05.033.

[42] H. D. Nelson, "A finite rotating shaft element using Timoshenko beam theory," *Journal of Mechanical Design, Transactions of the ASME*, vol. 102, no. 4, 1980, ISSN: 10500472. DOI: 10.1115/1.3254824.

[43] D. L. Thomas, J. M. Wilson, and R. R. Wilson, "Timoshenko beam finite elements," *Journal of Sound and Vibration*, vol. 31, no. 3, 1973, ISSN: 10958568. DOI: 10.1016/S0022-460X(73)80276-7.

[44] E. C. Bass, F. A. Ashford, M. R. Segal, and J. C. Lotz, "Biaxial testing of human annulus fibrosus and its implications for a constitutive formulation," *Annals of Biomedical Engineering*, vol. 32, no. 9, 2004, ISSN: 00906964. DOI: 10.1114/B:ABME.0000039357.70905.94.

[45] B. J. Bell, E. Nauman, and S. L. Voytik-Harbin, "Multiscale strain analysis of tissue equivalents using a custom-designed biaxial testing device," *Biophysical Journal*, vol. 102, no. 6, 2012, ISSN: 00063495. DOI: 10.1016/j.bpj.2012.02.007.

[46] G. A. Holzapfel and R. W. Ogden, "On planar biaxial tests for anisotropic nonlinearly elastic solids. A continuum mechanical framework," *Mathematics and Mechanics of Solids*, vol. 14, no. 5, 2009, ISSN: 10812865. DOI: 10.1177/1081286507084411.

[47] S. L. Omairey, P. D. Dunning, and S. Sriramula, "Development of an ABAQUS plugin tool for periodic RVE homogenisation," *Engineering with Computers*, vol. 35, no. 2, 2019, ISSN: 14355663. DOI: 10.1007/s00366-018-0616-4.

[48] S. M. Mirkhalaf, F. M. Andrade Pires, and R. Simoes, "Determination of the size of the Representative Volume Element (RVE) for the simulation of heterogeneous polymers at finite strains," *Finite Elements in Analysis and Design*, vol. 119, 2016, ISSN: 0168874X. DOI: 10.1016/j.finel.2016.05.004.

[49] H. KADOWAKI, G. HASHIMOTO, H. OKUDA, T. HIGUCHI, H. JINNAI, E. SETA, and T. SAGUCHI, "Evaluation of the appropriate size of the finite element representative volume for filled rubber composite analyses," *Mechanical Engineering Journal*, vol. 3, no. 5, 2016, ISSN: 2187-9745. DOI: 10.1299/mej.16-00372.

[50] W. M. Harris and W. K. Chiu, "Determining the representative volume element size for three-dimensional microstructural material characterization. Part 2: Application to experimental data," *Journal of Power Sources*, vol. 282, 2015, ISSN: 03787753. DOI: 10.1016/j.jpowsour.2015.02.052.

[51] M. S. Khan, S. S. Rahimian Koloor, and M. N. Tamin, "Effects of cell aspect ratio and relative density on deformation response and failure of honeycomb core structure," *Materials Research Express*, vol. 7, no. 1, 2020, ISSN: 20531591. DOI: 10.1088/2053-1591/ab6926.

[52] U. Gröschel-Stewart, M. Bardini, T. Robson, and G. Burnstock, "Localisation of P2X5 and P2X7 receptors by immunohistochemistry in rat stratified squamous epithelia," *Cell and Tissue Research*, vol. 296, no. 3, 1999, ISSN: 0302766X. DOI: 10.1007/s004410051321.

[53] Y. Shimoyama, S. Hirohashi, S. Hirano, M. Noguchi, Y. Shimosato, M. Takeichi, and O. Abe, "Cadherin cell-adhesion molecules in human epithelial tissues and carcinomas," *Cancer Research*, vol. 49, no. 8, 1989, ISSN: 15387445.